

Multi-level damage diagnosis on stiffened composite panels based on a damage-uninformative digital twin

Milanoski, Dimitrios; Galanopoulos, Georgios; Zarouchas, Dimitrios; Loutas, Theodoros

DOI

[10.1177/14759217221108676](https://doi.org/10.1177/14759217221108676)

Publication date

2022

Document Version

Final published version

Published in

Structural Health Monitoring

Citation (APA)

Milanoski, D., Galanopoulos, G., Zarouchas, D., & Loutas, T. (2022). Multi-level damage diagnosis on stiffened composite panels based on a damage-uninformative digital twin. *Structural Health Monitoring*, 22(2), 1437-1459. <https://doi.org/10.1177/14759217221108676>

Important note

To cite this publication, please use the final published version (if applicable).
Please check the document version above.


Copyright

Other than for strictly personal use, it is not permitted to download, forward or distribute the text or part of it, without the consent of the author(s) and/or copyright holder(s), unless the work is under an open content license such as Creative Commons.

Takedown policy

Please contact us and provide details if you believe this document breaches copyrights.
We will remove access to the work immediately and investigate your claim.

Multi-level damage diagnosis on stiffened composite panels based on a damage-uninformative digital twin

Structural Health Monitoring
2022, Vol. 0(0) 1–23
© The Author(s) 2022
Article reuse guidelines:
sagepub.com/journals-permissions
DOI: 10.1177/14759217221108676
journals.sagepub.com/home/shm


Dimitrios Milanoski¹ , Georgios Galanopoulos¹ , Dimitrios Zarouchas^{2,3} and Theodoros Loutas¹

Abstract

In this study, a multi-level Structural Health Monitoring methodology for stiffened composite panels is introduced. A digital twin (DT), that is, a three-dimensional finite element (FE) model, representing the pristine state baseline of the test article, is developed and verified for compressive loading in the post-buckling regime. The detailed FE model is utilized to train a surrogate model with respect to exogenous input, that is, axial load magnitude. The surrogate assists the DT concept that would allow prediction of the load acting on the structure based on an influx of strain data, acquired from fiber Bragg grating sensors permanently attached along the stringer feet. For this purpose, we leverage on the observation that remote from the damage, the strain field remains virtually unaltered with regard to the pristine state. The load is estimated by a sensor placed far from the damage whilst the diagnostic actions are performed by exploiting measurements from the remaining sensing locations. A health indicator, which compares the experimentally received strains with those from the surrogate representing the pristine state, is utilized to (1) detect, (2) localize, and (3) characterize the damage. As damage, we consider either skin-to-stringer disbond or initial impact damage propagation as well as overall stiffness degradation during thousands or millions of fatigue cycles. The sensors that have detected a disbond are dedicated to evaluating the potential propagation of it, while the remaining sensors evaluate the overall stiffness degradation. The proposed methodology is tested for one artificially disbanded and two impacted single-stringer panels subjected to block loading compression-compression fatigue.

Keywords

Structural health monitoring, damage diagnosis, digital twin, surrogate modeling, composite stiffened panels, fiber Bragg grating, fatigue

Introduction

The fast-evolving *digital twin* (DT) concept is constantly receiving a growing interest over the last years.^{1–3} The initial vision was oriented towards an alternative structural life prediction tool for predictive maintenance practices of aircraft vehicles.^{4,5} The conventional, and still ongoing, maintenance tasks of aircraft involve scheduled ground inspections after having operated a predefined number of duty cycles. The DT paradigm aims to reduce the extensive costs related to the scheduled ground inspections by providing diagnostic and prognostic forecasts onboard the flying vehicle.

Generally, we can define the DT as a digital replica of a real-world physical asset, that is, the physical twin (PT), capable of replicating the PT's behavior within a context of interest.^{6–8} The DT should be enriched with the best available physics-based models in order to mirror the performance of the PT.⁹ To achieve this scope, permanently

installed sensors will be transferring data to the DT in real-time communication between the twins. A fully integrated framework that enables this simultaneous update of the DT is also stated as “Digital Thread.”¹⁰

¹Laboratory of Applied Mechanics and Vibrations, Department of Mechanical Engineering and Aeronautics, University of Patras, Patras, Greece

²Structural Integrity and Composites Group, Faculty of Aerospace Engineering, Delft University of Technology, Delft, The Netherlands

³Center of Excellence in Artificial Intelligence for Structures, Prognostics & Health Management, Faculty of Aerospace Engineering, Delft University of Technology, Delft, The Netherlands

Corresponding author:

Theodoros Loutas, Laboratory of Applied Mechanics and Vibrations, Department of Mechanical Engineering and Aeronautics, University of Patras, Rio, Patras, Western Greece 26504, Greece.
Email: thloutas@upatras.gr

The recent advancements on computational efficiency allowed the utilization of high-fidelity numerical models, for example, finite element (FE) models, in response to the increased complexity of modern aerospace structures.¹¹ Conventional metallic aerostructures are perpetually substituted by inhomogeneous composite materials, for example, carbon-fiber reinforced polymers (CFRP), in favor of their unique specific mechanical properties. Yet, they are prone to unpredictable events resulting barely visible impact damages (BVID), which in turn may jeopardize their structural integrity, if not detected at an early stage. Aerospace structures are well-known for their damage-tolerant design which essentially means that damage is potentially present and allowed to grow slowly.^{12,13} However, it is vital to detect and monitor the development of such damage events in order to ensure a safe structural operation. Structural Health Monitoring (SHM) methodologies have been developed towards this demand. These methodologies may be further divided into two major categories, namely, (1) diagnostics and (2) prognostics. Actions related to the first category aim to provide insight about the presence, location, type as well as extent of the damage.¹⁴ Prognostics in turn perform predictions regarding the remaining useful life of the monitored structure.¹⁵ The DT concept is a promising approach for SHM that combines sensor data with a numerical model, for example, FE model, in order to interpret the underlying phenomena of damage evolution in the structure.

Moreover, the advent of machine learning brings new opportunities via surrogate, or so-called black-box, modeling.¹⁶ Currently, it is common to leverage on physics-based models (or white-box models^{8,17}), either in a theoretical¹⁸ or a numerical framework,¹⁹ to train a black-box model. The latter is fed by pairs of input-output (I/O) data, generated by the white-box models, mapping the output quantity of interest in a multidimensional feature manifold. Thus, operational, for example, boundary conditions, or state, for example, damage characteristics, information about the structure is embedded within a surrogate model, promptly available for predictions when an influx of input data is extracted from the PT. Hence, such a trained model maps the input variables to the observed output as well as generalizes its response to non-observed data. The learning stage of the black-box models is frequently conducted offline while only the evaluation of the model predictions is occurring during the online stage.^{20–22} This is important as the nature of the DT concept is closer to real-time SHM and thus, information must be rapidly processed.

Among the articles found in the literature about DT, we refer to some recent articles in the fields of structural analysis and SHM. Plenty of surrogate models are utilized, for example, artificial neural networks,^{23,24} convolutional neural networks,²⁵ Gaussian processes,^{26,27} generative adversarial networks,^{17,28} or others.

Significant effort has been given to fatigue damage diagnosis and/or prognosis of metallic or composite structures.^{19,21,23,24,26,29–31} The DT concept has been also used for diagnostic purposes on impact damage identification,³² while applications are also found in the field of wind energy structures subjected to fatigue loading.³³ A probabilistic DT framework of an offshore wind substructure was proposed by Augustyn et al.³⁴ The structural reliability of the substructure was assessed based on modeling the fatigue damage accumulation including various sources of uncertainty. The concept of DT is also finding applications in the field of marine engineering.^{35,36}

Strain-based SHM methodologies

As previously clarified, the data collected from a sensorized structure play a significant role for SHM applications. However, it is clear that sensors do not directly measure damage—Axiom IVa of SHM.³⁷

Several sensor types exist for a variety of SHM purposes. Fiber-optic sensors (FOS) are widely preferred for structural monitoring, both in research as well as industrial applications.^{38,39} FOS with engraved Bragg gratings⁴⁰ (FBGs) have several advantages, for example, extremely lightweight, low-power consumption, and immunity to electromagnetic interference. They can also measure dynamic strains apart from static ones. Moreover, FOS can be embedded in composite materials⁴¹ or directly affixed upon the surface of the host structure.⁴² Application at various structural complexities may be found in the literature, spanning from coupon level,^{24,43,44} or components with assembly details^{45–48} to more representative structures.^{49–54} Strain-based methodologies can also be divided in accordance with the nature of the interrogated strains, that is, dynamic^{55,56} or static.⁵⁷ In each case, proper post-processing of the multivariate uninformative raw strain data is required. For example, normalizing indicators may be used to reduce the dependency of strains on boundary conditions.^{20,45} However, if the boundary conditions are prescribed or estimated, direct strain comparison, between a reference (undamaged state-if available) and a potentially damaged one, may be used as a damage-sensitive indicator.^{46,52,58–60} Also, model-independent methodologies are followed where solely experimental data are utilized.^{61–65} Methods for damage identifications based on strains recorded from zero-strain trajectories are also employed.^{35,66,67} Lately, strain-based SHM methodologies utilizing the inverse FE method are emerging.^{68–70}

As previously mentioned, aerospace structures are designed under the principles of damage tolerance, operating under the existence and development of damage, intrinsic or induced, within their volume. However, it is of great importance to meticulously monitor the propagation of such damage as they may lead to catastrophic failure of the

structure. In the literature, model-based methods that inversely estimate the fatigue crack growth have been developed, but in most of the cases for unidimensional crack geometries. Similar damage morphologies seem to be idealized and not representative in more complex structural geometries, with multiple interfaces, like stiffened composite panels. Moreover, impact-induced damages produce a network of delaminations through the thickness of the impacted zone accompanied by other local damage types, for example, matrix cracking or fiber breakage, instead of unique delamination in the skin/stringer interface. Thus, it is common to observe planar (two-dimensional) delaminated areas with strong mixed-mode conditions along their fronts,¹³ especially under compression in the post-buckling regime. Stiffened panels are designed to sustain elevated loads^{71,72} and in some special cases the buckling instability is being deliberately exploited for morphing of composite wings.⁷³ Therefore, it is crucial to monitor these structural elements in order to mitigate sudden failure.

Methodology outlook

The present work introduces a multi-level diagnostic methodology for aeronautical composite single-stringer panels (SSPs) subjected to quasi-static (QS) as well as cyclic compressive loading conditions. Namely, three levels of SHM are envisaged: (i) damage detection, (ii) damage localization, and (iii) damage type classification. Artificial and impact-induced damage is considered for the current study. Leveraging on the modification of skin-to-stringer disbonds to the strain field, we develop a strain-based SHM methodology assisted by a DT of the pristine state of the structure. As the strains are highly affected in the vicinity of the damage, strains acquired far from damage remain virtually equivalent to those of the healthy structure. On this premise, we utilize the strain readings of one reference sensor in order to estimate the load acting on the structure via the DT, which is crucial for the subsequent feature extraction at every sensing location.

The first two SHM Levels are essentially implemented simultaneously, that is, damage is detected when the Health Indicator (HI) of a sensor exceeds a statistically-determined threshold; thus, damage localization is determined in the vicinity of the specific sensor. Next, based on the evolution of the HI, an extra effort is given to characterize the type of occurring damage. Hence, the third SHM Level is enabled via a sliding window algorithm which yields binary indications about

- (a) propagation of a detected disbond with respect to its nominal size,
- (b) overall (post-buckling) stiffness degradation.

The implementation of the DT-assisted methodology is realized using a computationally cheap surrogate model

which automates the load prediction, and thereupon the feature extraction. Load identification of highly-loaded structures is a usual SHM action.⁷⁴ The strength of the proposed methodology lies in the sole usage of simulated strains belonging to the pristine state, which in turn significantly reduces the computational demands associated with the numerical modeling campaign. However, the concept is not capable of quantifying the damage extent due to the lack of relevant training data. On the contrary, the diagnostic levels performed contain physical interpretation details that categorize two, different in nature, damage types. In-situ non-destructive testing (NDT) with an ultrasonic DolphiCam is performed to capture the propagation of the induced damage whilst data directly received from the test machine estimate the stiffness degradation. The limited cases of detached sensors are physically observed by eyesight in conjunction with the negligible strain readings recorded. The final agreement of the algorithm's performance with the experimental findings corroborates the potential of the proposed methodology. The conceptual methodology is schematically illustrated in Figure 1.

In the first section of the article, we present the experimental procedure followed. Then, the development of the DT is presented, incorporating the FE model and the training of the surrogate black-box model. The third section provides insight regarding the proposed DT-based damage diagnosis. The diagnostic levels are thoroughly discussed in the same section. The final section summarizes the findings of the proposed methodology and general conclusions are drawn.

In the present work, the crucial task of SHM on highly-loaded composite components is introduced based on the DT concept. The findings coming from three damaged SSPs empower the proposed methodology by efficiently detecting and localizing skin-to-stringer disbonds, as well as predicting further propagation of the disbonds in addition to overall stiffness degradation due to fatigue loading conditions.

Experimental campaign

Test articles

The SSP test articles are composed of three individual members, that is, skin, stringer, and cast-tabs. At first, the flat composite skin was co-cured with the T-section stringer. Then, two rectangular epoxy cast-tabs have been placed and cured at room temperature facilitating the compressive load introduction to the specimen. The cured panel was encased in the cast-tabs in a manner that the centroid of the skin/stringer cross-section coincides with the centroid of the tabs. A sensorized panel is shown in Figure 2(a) accompanied by the relevant dimensions in Figure 2(b). A graphite/epoxy material system IM7/8552 was used for both skin and stringer

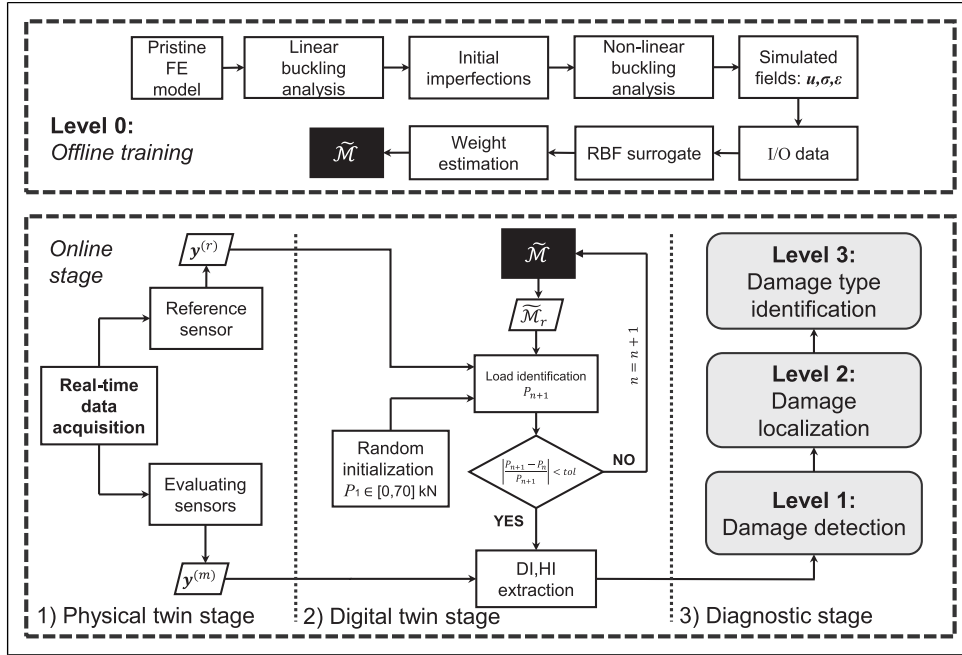


Figure 1. Schematic representation of the proposed methodology.

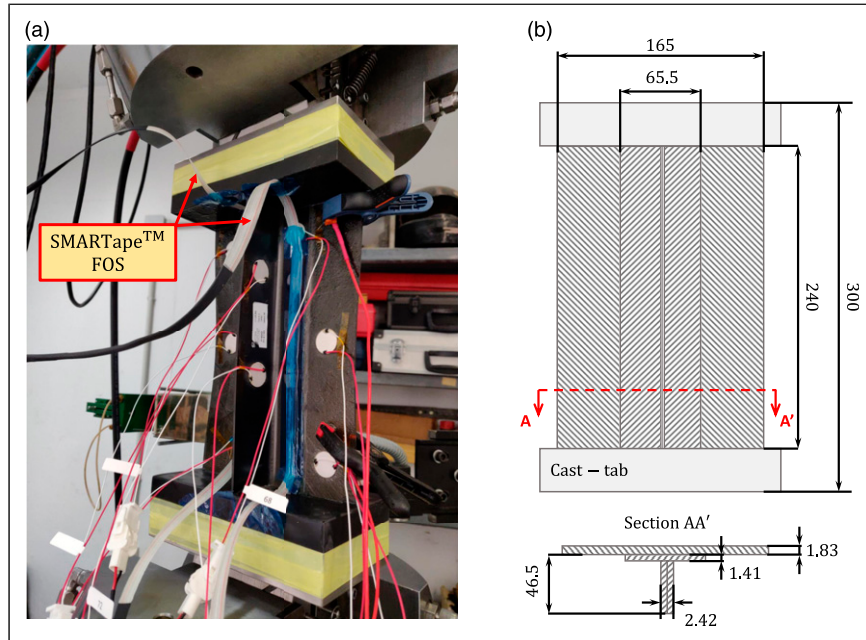


Figure 2. (a) Sensorized preview of the single-stringer panels (under buckling) and (b) its relevant dimensions expressed in mm.

with ply properties as shown in Table 1. The skin consists of 14 unidirectional continuum fiber-reinforced plies with a stacking sequence $[45/-45/0/45/90/-45/0]$ s whilst the stringer flange is composed by a 10-layer formation $[45/-45/0/-45/45]$ s. The cast-tabs were made by an epoxy resin AXSON®EPO 5019 with properties given in Table 2.

The composite panels were manufactured by OPTIMAL STRUCTURAL SOLUTIONS LDA (Alcabideche, Portugal). In total, two pristine specimens have been used for catastrophic QS tests whilst another three damaged specimens were tested in block loading compression-compression (C-C) fatigue, as described in the following sections.

Table 1. Elastic properties of IM7/8552.⁷⁵

Property	Value	Units
Longitudinal Young modulus, E_{11}	161,000	MPa
Transverse Young modulus, $E_{22} = E_{33}$	11,380	MPa
Poisson ratio, $\nu_{12} = \nu_{13}$	0.32	—
Poisson ratio, ν_{23}	0.45	—
Shear modulus, $G_{12} = G_{13}$	5200	MPa
Shear modulus, G_{23}	3900	MPa

Table 2. Material properties of EPO 5019.

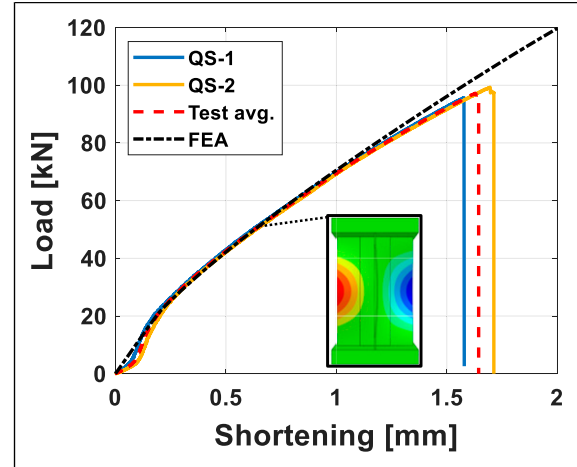
Property	Value	Units
Young modulus, E	6000	MPa
Poisson ratio, ν	0.3	—
Compressive yield strength, S_y^c	110	MPa

Quasi-static tests

Before conducting the fatigue tests, it is critical to estimate the failure load of the SSPs under compression. The total load that the panels withstood will dictate the operational limits of the subsequent fatigue loading. Two specimens, that is, QS-1 and QS-2, are subjected to QS compression upon failure with a constant displacement rate of 0.5 mm/min. All of the specimens were tested in the facilities of the Applied Mechanics Laboratory, University of Patras. A servohydraulic INSTRON 8802 test machine with load capacity ± 250 kN was utilized. The actual shortening between the two tabs is measured via a linear variable differential transformer which was properly fixed upon the tabs. The load-shortening curves of the two panels are presented in Figure 3. Initially, a linear relation between the load and the panel's shortening is developed upon the buckling load, approximately at 20 kN. After this point, a nonlinear regime follows along a path with reduced stiffness compared to the initial linear slope. The nonlinear behavior on the structural response is associated with a geometric nonlinearity source, as the out-of-plane displacements become significantly large when the bifurcation point is reached. The collapse load for QS-1 and QS-2 was found 95.6 and 99.3 kN, respectively. The response of the SSPs is in accordance with the findings of the numerical elastic solution. In Section "Digital twin development," the FE model is developed and further discussed.

Block loading C-C fatigue

The concept of the proposed methodology is implemented via a block loading C-C fatigue test, with constant amplitude (CA) per block, for the case of three damaged SSPs. The maximum limits of the fatigue blocks were selected

**Figure 3.** Load-shortening curves.

according to the collapse load to avoid instant failure of the specimen. The panels are subjected to sinusoidal cycling load between a range $[P_{\min}, P_{\max}]$, stress ratio $R = 10$, and a frequency $f = 2$ Hz. Throughout the test campaign, the load limits have been judiciously increased on occasions when no further propagation of the damage was observed. Details about the fatigue block limits, the number of fatigue cycles until total failure as well as the damage characteristics on each specimen are summarized in Table 3. Cyclic-load excitation was imposed for 500 consecutive cycles until a QS test was intervened; the test intervals are vital for the current methodology as strain data acquisition via FBGs was made during that period. Each QS test, besides the first one, initiates from a minimum load, $P_0 = -5$ kN, upon the maximum limit of fatigue at the relevant period, P_{\max} , with a constant displacement rate of 0.5 mm/min. The test plan is schematically presented in Figure 4.

Specimen CA-1 contains an artificial disbond in the skin/stringer interface using a Teflon insert. CA-2 and CA-3 specimens were impacted in the facilities of the laboratory with an in-house drop tower apparatus. BVID damage occurred in both specimens; the one with impact energy 7.4 J left no trace of damage in the impact zone whilst the specimen hit with 10 J revealed a small dent. Further specifications about impact damages are presented in the section "In-situ non-destructive evaluation." The tests are concluded with the collapse of the SSPs.

Strain sensing

Every SSP is equipped with two commercial FOS SMARTAPETM, with five FBGs per tape, provided by SMARTEC S.A. (Switzerland). The 10-mm gratings were made along the fibers with a spacing approximately equal to 30 mm. Two thin glass-epoxy layers accommodate the optical fibers, protecting the sensors from the ambient

Table 3. Details of the block loading fatigue tests and damage specifications per panel.

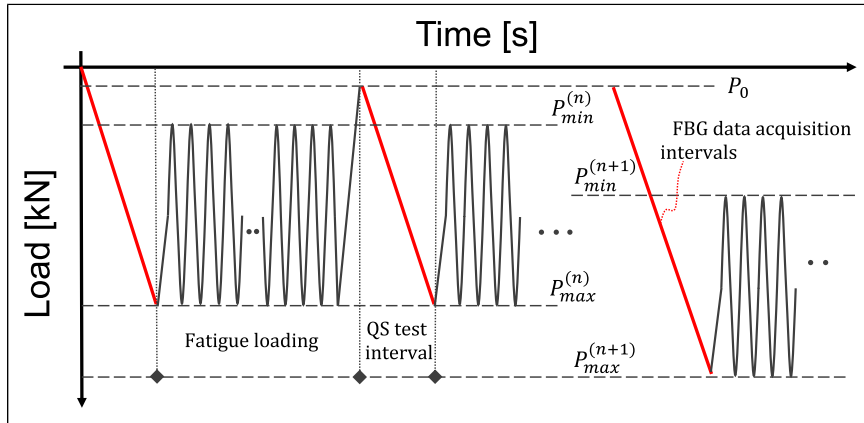
SSP	Damage type*	Damage location** [x,z] (mm)	Initial damage area(mm) ²	P _{min} (kN)	P _{max} (kN)	Consecutive cycles	Failure cycles
CA – 1	D – 30×30 mm ²	[15,210]	901.5	–3.5	–35.0	10,000	345,000
				–3.9	–39.0	10,000	
				–4.5	–45.0	10,000	
				–5.0	–50.0	170,000	
				–5.5	–55.0	85,000	
				–6.0	–60.0	60,000	
CA – 2	I – 10 J	[22.5200]	1397.9	–4.0	–40.0	10,000	217,000
				–4.5	–45.0	177,000	
				–5.0	–50.0	30,000	
CA – 3	I – 7.4 J	[32.5105]	232.5	–4.0	–40.0	10,000	243,000
				–4.5	–45.0	80,000	
				–5.0	–50.0	90,000	
				–5.5	–55.0	63,000	

* I: impact
damage

D: artificial
disbond

**with respect to the coordinate
system shown in Figure 7

Note: SSP: single-stringer panels.

**Figure 4.** Test plan definition.

environment as well as easing the handling of the tape upon the host material without danger of fiber rupture. The sensor tapes were mounted on the stringer feet along the longitudinal direction via a secondary bonding technique. A copolyamide GRILTEX[®] flexible adhesive was utilized to adhere the tapes to the panels. The locations of every FBG along the feet of the panels are displayed in Figure 5. The central sensor per tape was approximately placed at the midspan of each foot. Only for the case of CA-1, the sensor tape was deliberately mounted on the foot in a manner that FBG-1 and FBG-2 lie above the fronts of the disbond, as shown in Figure 5. This action assists the assessment of the modified strain field along the disbond, as it will be presented in the section “Effect of skin-to-stringer disbond.”

The experimental longitudinal strains were acquired using a 2-channel MICRON OPTICS INC. SM130 dynamic

interrogator with recording capabilities up to 1 kHz. The interrogator receives the reflected spectrum by the inscribed gratings of each sensor. The reflected light travels with the Bragg wavelength based on the Bragg equation

$$\lambda_B = 2n_{\text{eff}}\Lambda_B \quad (1)$$

where n_{eff} is the effective refractive index and Λ_B is the grating period. As the optical fiber is properly affixed upon a host material, the optical fiber follows the deflection of the host material. Thus, the fiber is dilated or compressed, which in turn, modifies the effective refractive index and the Bragg period, leading to a shift on the wavelength according to the next relation:

$$\frac{\Delta\lambda_B}{\lambda_B} = (1 - p)\varepsilon_{11} \Rightarrow \varepsilon_{11} = \frac{\Delta\lambda_B}{\lambda_B} \cdot f_g \quad (2)$$

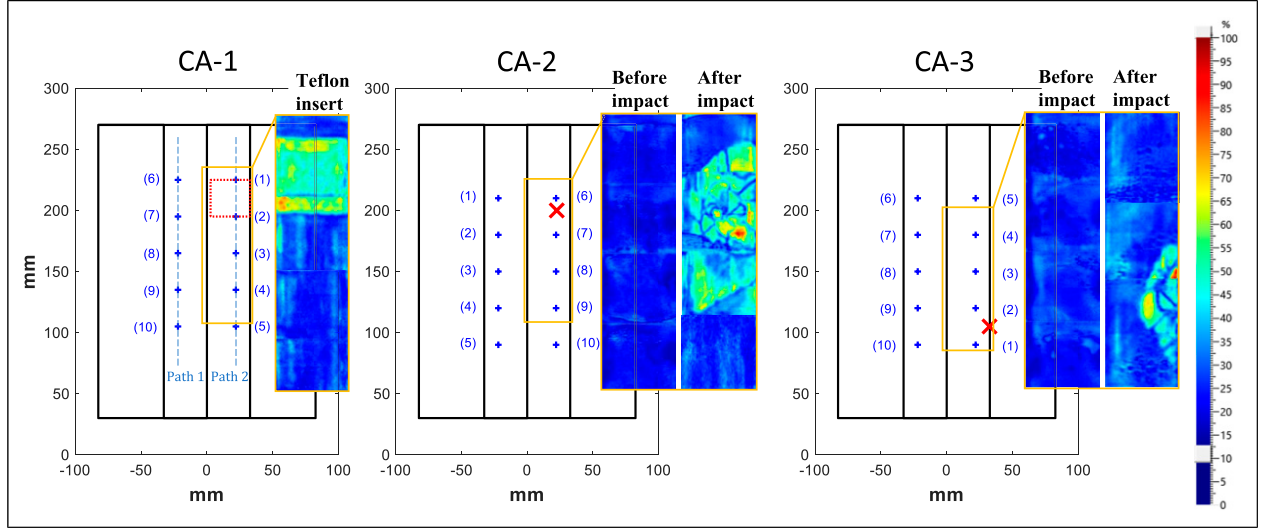


Figure 5. Initial artificial and impact damage configurations as evidenced with phased-array ultrasound. Blue plus signs (+) represent the Fiber-optic sensors with engraved Bragg gratings positions. Contour plot indicates the intensity of the maximum value of the reflected pulse.

with p representing the photoelastic coefficient and ε_{11} is the axial strain along the fiber. The induced fiber strain is also affected by temperature variations that cause thermal elongation of the fiber, and therefore modify the Bragg period as well as the refractive index. However, the test conditions remained constant at room temperature, and thus, we neglect the temperature contribution. For the FOS used, the manufacturer provided a gauge factor $f_g = 1.2$ which transforms the relevant wavelength shift to strain.

In-situ non-destructive evaluation

In order to evaluate the effectiveness of the methodology, it is important to inspect the SSPs via NDT techniques. A phased-array ultrasound system, that is, DolphiCam, dedicated to inspection on CFRP, was used. DolphiCam incorporates a variety of inspection techniques, for example, A-, B-, and C-Scan.

In the current framework, C-Scan inspections were conducted in several occasions during pauses of the testing operation. The amplitude of the reflected pulse was selected to illustrate the measurements from the phased-array camera. The scanning region of the camera is a $30 \times 30 \text{ mm}^2$ rectangle area. Measurements have been taken by the side of the flat skin in the proximity of the damaged area. For the two impacted panels, it was found that the impacts caused skin-to-stringer delamination as well as delaminations among the plies of the skin. This can be identified via the color variations based on the inspection images presented in Figure 5. For the case of CA-3, we are only concerned with the induced delaminated area beneath the skin/stringer interface, as the impact also affected the

skin region outside the latter interface. Figure 6 summarizes the disbonded area as measured for all the specimens during the test campaign. The initial measurement of the nominal damage extent is reported in Table 3.

Digital twin development

In the section herein the DT development, as well as its key role, are introduced. As mentioned before, we consider a FE model representing the healthy structure with the absence of any initial or developing damage. After verifying the FE model, we proceed to its substitution by a surrogate model, which is trained with I/O pairs generated by the FE model.

Finite element model

For the needs of the numerical modeling, the commercial⁷⁶ FE package ABAQUS/CAE 2021TM was utilized. The FE model of the SSP is shown in Figure 7. The geometry of the specimen is explicitly designed apart from the small filler (resin rich) region in the root of the stringer. Four separate members are created, that is, the flat skin, the stringer flange, the stringer web, and the two epoxy tabs. Kinematic restraints were imposed in terms of tie constraints, in the regions where two parts were fixed to each other, as highlighted in Figure 7. The composite skin and stringer parts are modeled using 8-node hexahedron continuum shell elements with reduced integration (SC8R). Each part was discretized with an approximate global mesh size of 1.25 mm. The two cast-tabs were modeled using general-purpose three-dimensional brick elements, with eight nodes, a reduced integration scheme (C3D8R), and 4.00 mm global

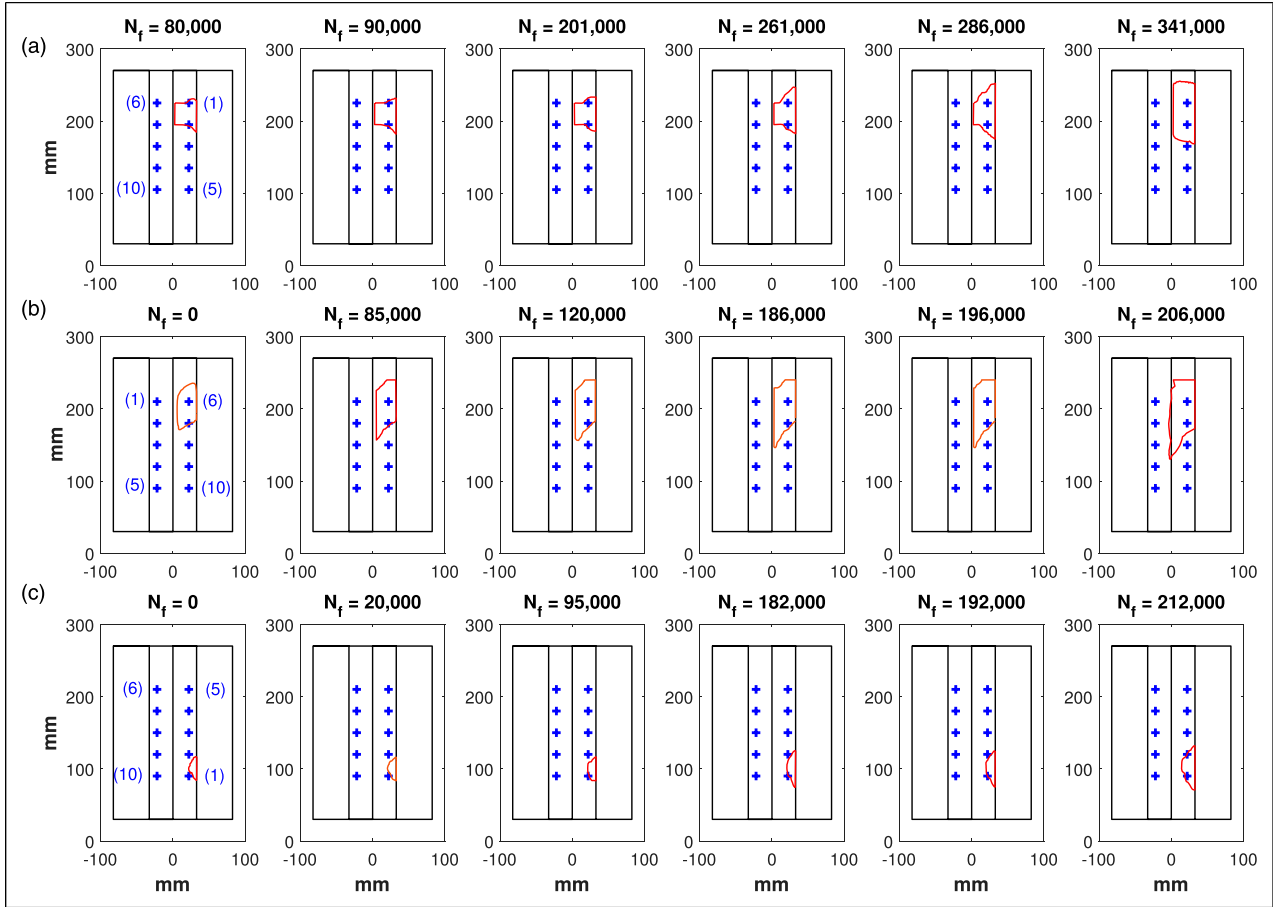


Figure 6. Propagation of skin-to-stringer disbond throughout the test span as estimated from phased-array ultrasound measurements for (a) CA-1, (b) CA-2, and (c) CA-3 specimens.

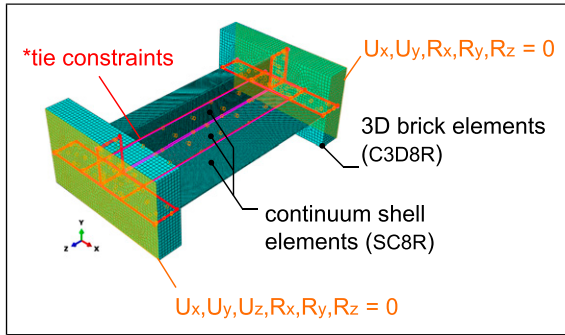


Figure 7. Digital twin - 3D FE model of the test article.

mesh size. A total mesh size of 158,400 and 19,984 SC8R and C3D8R elements, respectively, was generated. The boundary conditions have been imposed to the outer surfaces of the two cast-tabs as shown in Figure 7. The constitutive model of the composite plies was modeled as elastic with transversely isotropic material properties as presented in Table 1. As previously stated, initiation or

progression of inter- and intra-laminar damage is not included in the analysis. The cast-tab material was also defined as elastic isotropic with respect to the properties of Table 2. The induced compressive stresses in the tabs were significantly lower than the compressive yield strength given by the material datasheet, and thus, elastic consideration of the tab material is valid. Namely, for a 70 kN imposed compressive load, maximum compressive stress equal to 16.3 MPa was obtained from the loading tab.

The numerical analysis is divided into two steps. Initially, the first step performs a linear perturbation analysis in order to estimate the buckling eigenvalues and their corresponding mode shapes. Generally, the mode shapes, expressed as a normalized nodal displacement field along the surfaces of the geometry, are used as initial imperfections that facilitate the nonlinear buckling analysis. This method prevents the analysis from numerical instabilities as the structure approaches the bifurcation point, and frequently, a sensitivity analysis is conducted to deduce how many modes should be incorporated. In the considered panel, verified also by the initial QS tests, the most dominant

mode shape during buckling is the first one, forming a half-wave along both sides of the skin, as shown in Figure 3. Thus, only the first buckling mode shape is selected as a scaled (5% of skin thickness) imperfection field. The solution of the nonlinear analysis is enabled with the Newton-Raphson solver incorporating large displacements formulations.

The load-shortening curve of the elastic numerical analysis is presented in Figure 3, along with the experimental evidence. Longitudinal strains are extracted from the top surface of the stringer feet by discrete element sets at the corresponding regions where real FBGs are installed. For that purpose, a Python script was utilized; each set consisted of three elements and the average strain of the elements was obtained. Verification on the strain readings is made utilizing data from early test intervals of CA-1 during the first 63 QS tests, that is, 21 from -35 kN, 21 from -39 kN, and 21 from -45 kN. More specifically, strains from the five FBGs along the bonded foot are compared to the simulated strains of the healthy model yielding average (absolute) errors of 4.96%, 0.63%, 5.39%, 1.81%, and 2.09% for FBG-6, FBG-7, FBG-8, FBG-9, and FBG-10, respectively. The agreement between experimental and numerical strains supports the assumption that remote from damaged regions, the strains remain unaltered. Further insight is provided in the section “Effect of skin-to-stringer disbond.”

Surrogate modeling

The numerical model created in the previous section is used to produce a baseline for the pristine state of the structure. Leveraging this baseline, the multi-level damage diagnosis will be implemented with experimental strain data acquired from the PT of the SSP. The response of the DT is embedded in a surrogate black-box model which maps the output strains of the DT, \mathbf{y} , in the multidimensional space of the state vector \mathbf{X} . Hence, $\mathbf{X} = \{\mathbf{x}^{(i)}, \mathbf{z}^{(i)}, \mathbf{P}^{(i)}\}_{i=1}^N$, where $x^{(i)}, z^{(i)}$ refer to the FBGs coordinates at their relevant locations and P refers to the load magnitude. It is clear that the damage-free baseline is illustrated with the latter state vector, which only contains details about the load. A supervised learning approach based on Radial Basis Function (RBF) models is followed. The sensing locations were slightly varying among the panels as the SMARTAPETM were manually placed. Thus, three different surrogates are utilized here, one for each panel based on the corresponding locations of the sensors x, z . Each surrogate is fed with a total array of $N = 1040$ strain values, expressed as $\{\mathbf{X}^{(i)}; \mathbf{y}^{(i)}\}_{i=1}^N$ combinations that correspond to 104 load subdivisions within the range $[0, 70]$ kN, acquired from $N_s=10$ FBGs. The input variables have been normalized in the space of a unit cube $[0, 1]^3$ to avoid scale effects on the data. The RBF surrogate is being developed and available in MATLAB environment.¹⁶ The approximation of the DT model, $\tilde{\mathcal{M}}$, obeys the following

interpolation conditions, for a parametric or fixed basis function ψ :

$$\tilde{\mathcal{M}}(\mathbf{X}^{(j)}) = \mathbf{w}^\top \boldsymbol{\psi} = \sum_{i=1}^{N_c} w_i \psi(\|\mathbf{X}^{(j)} - \mathbf{c}^{(i)}\|) = \mathbf{y}^{(j)} \quad (3)$$

where $j = 1, \dots, N$ and N_c are the number of the basis functions centers $\mathbf{c}^{(i)}$. The RBF formulation resembles a linear single-layer neural network with input \mathbf{X} , hidden units $\boldsymbol{\psi}$, weights \mathbf{w} , and output \mathbf{y} . The weight estimation is conveniently simplified when the centers coincide with the data points, that is, $\mathbf{c}^{(i)} = \mathbf{X}^{(i)}$, yielding:

$$\boldsymbol{\Psi} \mathbf{w} = \mathbf{y} \Leftrightarrow \mathbf{w} = \boldsymbol{\Psi}^{-1} \mathbf{y} \quad (4)$$

where, $\boldsymbol{\Psi}_{i,j} = \psi(\|\mathbf{X}^{(i)} - \mathbf{X}^{(j)}\|)$, is the Gram square matrix. A fixed basis function, that is, thin plate spline $\psi(\rho) = \rho^2 \ln \rho$, is utilized. Half of the data were used as test set, leading to root mean square error RMSE between the predictions and the target strains equal to $1.21 \mu\epsilon$, indicatively for CA-1.

Digital twin-assisted diagnostic methodology

Having trained the surrogate models that substitute the FE numerical model, the way is paved for the DT-assisted damage diagnosis. Hereinafter, the surrogate model represents the DT whilst the PT is being monitored during service/loading.

Effect of skin-to-stringer disbond

The main concept behind the proposed methodology is based on the premise that a discontinuity alters the strain field in its proximity. Indeed, the new surfaces created around a discontinuity, for example, skin/stringer disbond, redistribute the stresses/strains which are intensified in its adjacent region. To illustrate the strain modification around a disbond, we utilize the verified numerical model, incorporating now a 30×30 mm² skin/stringer disbond along Path 2. The disbond is modeled as a surface where no relative restrictions are applied in the kissing nodes. Also, the “Hard contact” definition was introduced to avoid interpenetration between the disbonded surfaces. Then, the top surface longitudinal strains are extracted from the highlighted region, which represents the region where the SMARTAPETM was placed, as shown in Figure 8. To quantify the divergence between the pristine and the damaged case, a HI is utilized as:

$$\text{HI} = \left| \frac{\epsilon_p - \epsilon_d}{\epsilon_p} \right| \quad (5)$$

where ϵ_p (Figure 8(a)) and ϵ_d (Figure 8(b)) denote the strains from pristine and damaged states, respectively. Moreover,

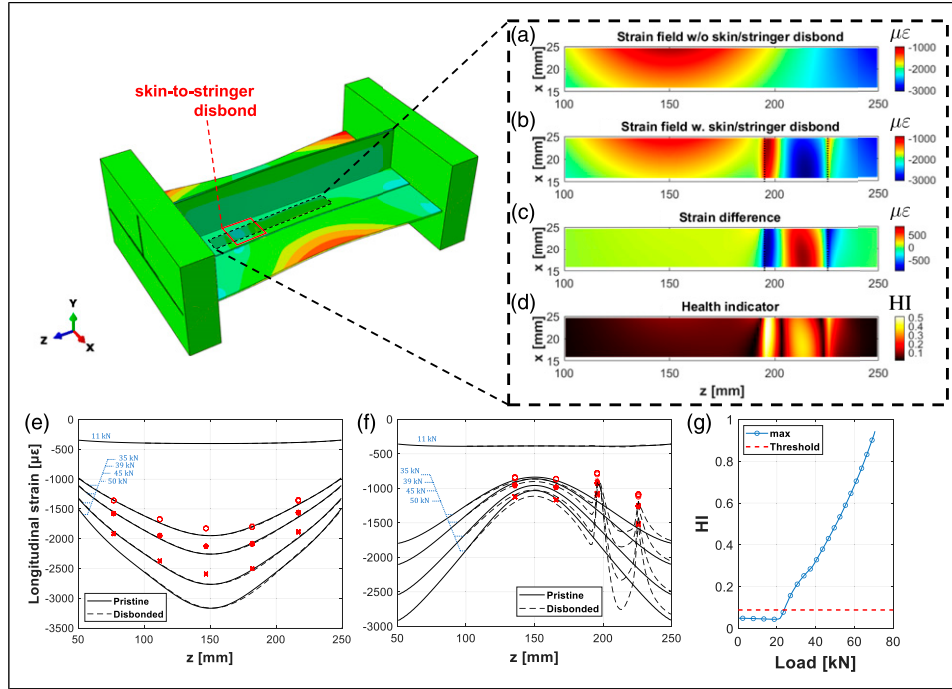


Figure 8. Simulated strain field at (a) pristine and (b) disbonded state, (c) strain difference between the two states and (d) HI field, at -50 kN compressive load. Numerically estimated strain distributions along (e) Path 1 and (f) Path 2 as highlighted in Figure 5, versus actual FBG measurements at -35 kN (\circ), -39 kN (\ast), and -45 kN (\times). (g) Max. value of HI with respect to load.

the strain modification is severely affected by the load magnitude and rises when the latter does. Generally, we can observe that the strain modification is mainly developed in the disbond fronts as well as in the middle of its length. More specifically, the strain along the longitudinal direction of the disbonds presents a peak-valley-peak profile,^{57,63} as shown in Figures 8(c) and (d). Figures 8(e) and (f) present the numerical strain distributions along Path 1 and Path 2, as previewed in Figure 5, accompanied by the strain measurements recorded during the first 63 QS tests from CA-1. The solid and dashed lines represent the strain distributions of the pristine and the disbonded model, respectively. Along Path 1, the numerical strain distribution of the pristine as well as of the disbonded model is roughly identical, as the disbond is placed along Path 2. The agreement among the observations and the simulated (healthy) strains has been previously quantified, in the “Finite element model” section. The good agreement between the FBG measurements along Path 2 with those of the disbonded FE model supports the premise of localized strain disturbance solely in the vicinity of the damage. The dependence of the HI to load is realized by gathering the maximum observed HI values along the highlighted region, at various loads. The relevant values are depicted in Figure 8(g), in conjunction with the detection threshold defined in section “Diagnostic levels.” It is obvious that the methodology is able to detect the presence of a

disbond when the panel is subjected to compressive loads greater than the buckling load. Below the buckling load, approximately, the strains differences between pristine and damaged state become significantly lower. However, the detection limit also depends on the disbond size; here, we have indicatively illustrated the case of a 30×30 mm² rectangle disbond.

Stiffness degradation

As the fatigue loading progresses, the material properties are decreasing and overall stiffness degradation of the panel is observed.⁷⁷ As this mechanism occurs, the strains are affected if compared to the nominal condition. Thus, it is expected to observe strain field modification, in a much lower extent compared to the disbond effect, though. In cases that the two damage types, that is, skin/stringer disbond and stiffness degradation, co-exist, it is hard to distinguish the partial contribution of each one. In order to visualize the global effect of stiffness degradation to the strain field, we perform the same buckling analysis for the case of the pristine model having longitudinal Young modulus decreased by an exemplary 7% with respect to its nominal value. In Figure 9, the ratio of the two strain fields, $r_\epsilon(x, z) = \frac{\epsilon_n(x, z)}{\epsilon_{sd}(x, z)}$, is presented, with ϵ_n denoting the strains with the initial E_{11} whilst ϵ_{sd} the strains for the case of a

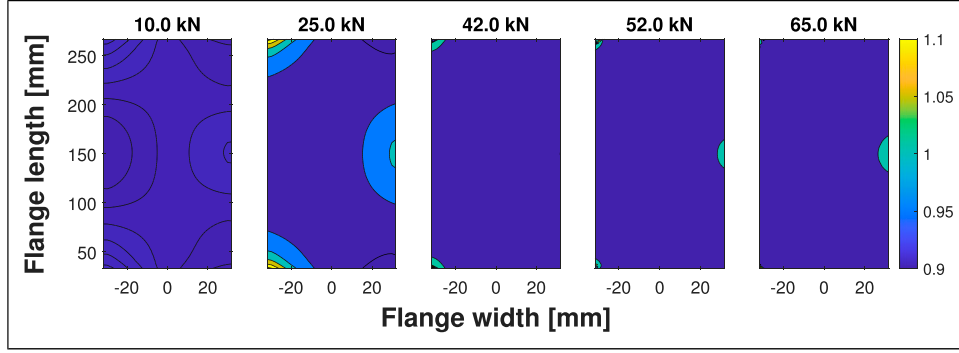


Figure 9. (a) Longitudinal strain field ratio r_e at the top surface of the stringer flange.

modified modulus as $0.93E_{11}$. The deviation between the two states can be clearly noticed in the total area of the stringer foot.

Load identification

In the current section, the monitoring feature, which will be used throughout the test campaign, is introduced. The HI defined in equation (5) is selected for this purpose. This indicator quantifies the deviation from the pristine baseline, ε_p , which in this framework is given by the DT. The term ε_d represents the experimentally acquired strains. However, it is noted that utilization of this indicator should be wisely made only under the knowledge of the boundary conditions, otherwise, irrelevant strains will be compared, leading to erroneous interpretations. In this study, the compressive load is the only variable boundary condition. Based on the findings from the previous subsections, the negligible strain modification, developed remote from the damage, is exploited for the needs of load identification. Figure 10 presents a solid body with arbitrary geometry, which helps to perceive the DT concept.

We can abstractly say that strains in a close domain near to the discontinuity, Ω_d , will be disturbed, if compared to the equivalent domain in the absence of the discontinuity. In contrast, the strains outside this domain can be considered as practically equal, $\varepsilon(\mathbf{x}_r) \approx \varepsilon(\mathbf{x}_p)$, with $\mathbf{x}_r \in \Omega_r$ and $\mathbf{x}_p \in \Omega_p \cap \Omega_r$ and position vector for the i_{th} point defined as $\mathbf{x}_i = \{x_1^{(i)}, x_2^{(i)}, x_3^{(i)}\}^T$. Concretely, we can support that in the domain $\Omega_p \cap \Omega_r$, the body without the discontinuity mirrors the behavior of the body with discontinuity, enclosed in Ω_d , and thus, it can be treated as a twin.

In this condition, a reference sensor, placed at $(x^{(r)}, z^{(r)})$ with respect to the Cartesian system shown in Figure 8, would be dedicated to estimate the load based on the experimental strain measured. Hence, the DT adapts its behavior to the strain reading coming from the PT. The load will be determined by minimizing the following squared ℓ^2 -norm objective function F :

$$P = \underset{P}{\operatorname{argmin}} \left\{ \underbrace{\|\tilde{\mathcal{M}}(x^{(r)}, z^{(r)}, P) - \mathbf{y}^m\|^2}_{\equiv F(x^{(r)}, z^{(r)}, P)} \right\} \quad (6)$$

where \mathbf{y}^m is an experimentally measured strain whilst $\tilde{\mathcal{M}}(x^{(r)}, z^{(r)}, P) \equiv \tilde{\mathcal{M}}_r$ is the DT's deterministic strain prediction, at load P . The load is iteratively predicted utilizing the steepest (gradient) descent method:

$$P_{n+1} = P_n - \gamma \frac{\partial F}{\partial P} \quad (7)$$

with step size γ . The derivative term of the objective function is numerically computed using central differences:

$$\frac{\partial F}{\partial P} = \frac{1}{\epsilon} [\tilde{\mathcal{M}}(x, z, P) - \mathbf{y}^m] \cdot [\tilde{\mathcal{M}}(x, z, P + \epsilon) - \tilde{\mathcal{M}}(x, z, P - \epsilon)] \quad (8)$$

where ϵ is a small perturbation. So, each time the load is determined by sacrificing the reference sensor, the HI is predicted for the remaining FBGs, as shown in the methodology flowchart in Figure 1.

Diagnostic levels

Level 1: Damage/anomaly detection. In the first level, the identification of a skin/stringer, or general delaminated region, will be evaluated using the HI. In section “Effect of skin-to-stringer disbond,” the behavior of this indicator was proved to be sensitive to the existence of such a type of damage. However, the definition of a threshold is crucial to efficiently classify the damage presence, in cases that the HI values exceed the threshold. As the HI (see equation (5)) correlates the DT's strains, that is, ε_p , with those of the PT, that is, ε_d , the threshold should encompass the intrinsic deviation between the calibrated numerical model and the experiment. This action incorporates the epistemic error as well as the aleatoric uncertainty related to the experimental

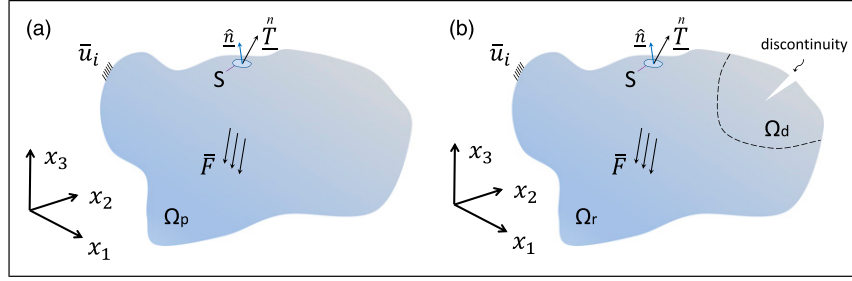


Figure 10. Prismatic solid body (a) w/o and (b) with the presence of a discontinuity, subjected to body forces \bar{F} , surface tractions \bar{T} , and boundary conditions \bar{u}_i .

measurements. The DT predictions are deterministic; in order to account for the aleatoric uncertainty of the strain measurements, the simulated strains are contaminated with Gaussian noise, with zero mean and a variance, $\varepsilon_{GN} = \varepsilon_{FEM} + \mathcal{N}(0, \sigma_m^2)$. To properly determine the threshold value, we form a HI database that corresponds to the pristine conditions.^{78,79} Strains acquired from the FBGs located along Path 1 (see Figure 5), that is, FBG 6–10, of CA-1 are considered. Even if CA-1 includes a disbond along the Path 2, the strains along Path 1 were found to resemble the pristine state as they were unaffected by the presence of the disbond (Figure 8(e)). The global threshold definition steps are presented below:

1. Experimental strains are recorded from CA-1 during the initial 63 QS tests. The 63 tests are split into three groups containing load limits from -5 up to -35 , -39 , and -45 kN, respectively.
2. The static strains at maximum compressive load are stored per FBG sensor $\rightarrow [y_m]_{63 \times 5}$ (the first 21 recordings are shown in Figure 11 with red marks).
3. From the total population of the received strains the variance, σ_m^2 , per FBG is calculated.
4. Noisy samples of the simulated strains, are formed per FBG location based on the previously estimated variance, for each load limit $\rightarrow [\varepsilon_{GN}]_{1000 \times 5}$ (see blue signal in Figure 11).
5. HI samples are constructed per FBG, based on the noisy numerical samples and the experimental strains $\rightarrow [HI]_{63,000 \times 5}$.
6. All values of the HI samples, from every FBG, are used to estimate the empirical cumulative distribution function (ecdf).
7. By setting 98% confidence intervals (CI) to the predefined ecdf, the threshold is set equal to its top bound.

The threshold value was found to be **0.089**, derived from the ecdf shown in Figure 11(a). Also, steps 1–5 are depicted in Figure 11(b), indicatively for strain data coming from the first 21 QS tests. The confidence level

approximately guarantees that from 100 independent experiments, two of them may produce a false positive. The described approach specifies the threshold value, which is essential to diagnose the presence of damage. Strains utilized from an a priori damaged specimen, though, acquired from a damage-unaffected region, are exploited to estimate the inherent discrepancy between the simulated and the experimental strains. Hence, the need for experimentally testing a pristine structure, here, is eliminated. Moreover, the SSP during the period that the strains were received, experienced 30,000 cycles of fatigue, with no significant stiffness degradation as will be presented in the “Results and discussion” section. Also, no evidence of disbond propagation was found from non-destructive inspections, something which is necessary, as it may have produced biased data.

One more source of anomaly, besides skin/stringer disbond, is the potential detachment of a sensor from the host material. The urge of detecting this type of anomaly was mainly developed after observing the evidence of the experimental campaign. Some regions along the tape were revealed to be vulnerable. That is at the end of the bonding length, as there, the tape is bent due to the presence of the loading tabs. Some limited cases were observed by eyesight when a color deviation was noticed in the region where the tape was disbonded. This is feasible as the sensor tape is made of two thin glass-epoxy layers, which are virtually transparent. If a sensor’s bonding is compromised, the tape loses its ability to stretch/compress in accordance with the host material, and thus, the strains are not properly transmitted from the latter to the tape. Hence, it is expected that such a case would yield insignificant strain readings, and subsequently elevated values of HIs. So, the concept behind detecting potential detachment is oriented towards sensors producing large HI values, and remains unaltered for a sustained period of time. A fixed threshold for the large values of HI was judiciously specified equal to 0.75, as it is not expected to observe that large HIs solely attributed to disbond presence, especially within the operational condition tested in the current analysis. For instance, recall from Figure 8(g) that the maximum observable HI is equal to 0.75

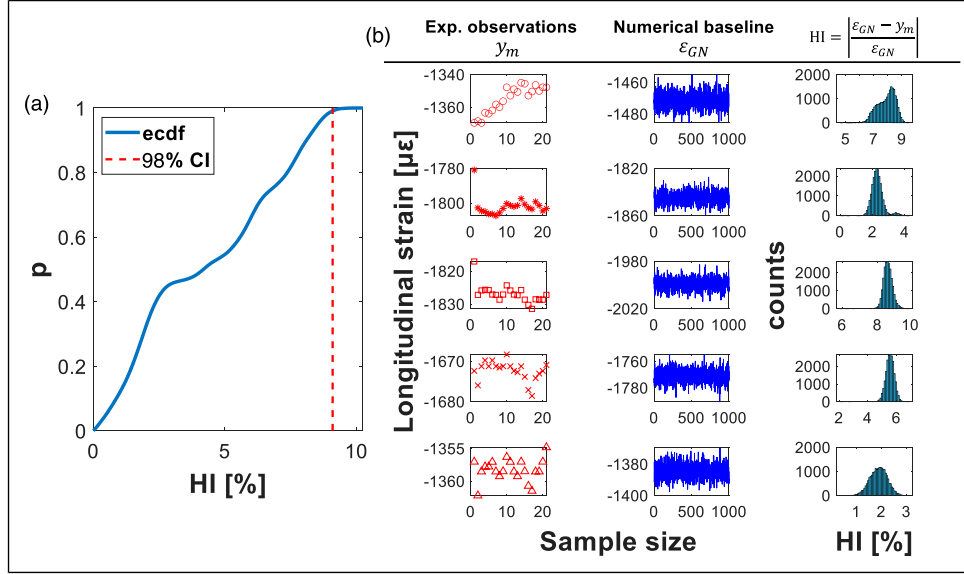


Figure 11. (a) ecdf of HI and (b) experimental strains, simulated strains with Gaussian noise and calculated HI samples at -35 kN. FBG-6 (\circ), FBG-7 (\ast), FBG-8 (\square), FBG-9 (\times), FBG-10 (\triangle). Note: FBG: Fiber-optic sensors with engraved Bragg gratings.

at load level -63 kN. The last condition was realized as 10,000 consecutive fatigue cycles. If these three conditions are fulfilled, the sensor is declared as detached and no further data post-processing is conducted for this sensor.

Level 2: Damage localization. The localization of damage in the current study is implemented using the HI at every sensing location. Hence, when the HI exceeds the pre-defined threshold, a binary damage index (DI) is generated:

$$DI_i = \begin{cases} 1, & \text{if } HI_i > 0.089 \\ 0, & \text{if } HI_i \leq 0.089 \end{cases} \quad (9)$$

with $i = 1, \dots, N_s$ denoting the relevant FBG sensor. Whenever the DI is equal to 1, damage/anomaly is detected, and at the same time localized, based on the sensor that satisfies this condition.

Level 3: Damage type identification. The last stage of the present damage diagnosis concept deals with damage type identification. Namely, two types are investigated: (i) *propagation* of a previously detected disbond and (ii) *post-buckling stiffness degradation*. Different techniques are used to estimate which type of damage is developing throughout the test span. Based on the observations made in the previous sections, it is expected that an increase on the boundaries of a disbond would, in turn, affect the behavior of the HI. This is attributed to the modified strain field (see “Effect of skin-to-stringer disbond”); a strain signature characterizes the damage morphology, and any time the damage propagates, the morphology modifies its

boundaries, and in turn, the HI alters its values, especially when a sensor is placed in the proximity of the damage. The level of damage complexity, though, does not guarantee a monotonic behavior, as the strain modification entails both increases and drops with respect to the pristine strain field (see Figures 8(c) and (d)).

(i) Thus, for the case of disbond propagation, the HI behavior was exploited, only for the sensors labeled as damage affected, that is, $DI = 1$. This is quite straightforward, as it is more likely that sensors already close to damage will be affected by an imminent propagation of the nominal damage. Next, a sliding window methodology, in accordance with Broer et al.,⁶³ was followed to detect changepoints on the HI. As the test continues, each of the damage-affected HIs is monitored and its data processed based on the sliding window approach, as shown in Figure 12(a). More specifically, a reference window stores the HI values and estimates the boxplot statistics, namely, median, μ_R , first quartile, Q_1 , and third quartile, Q_3 . The reference window contains data acquired from 2500 cycles, or equivalently five intervals, at instances t_0, \dots, t_R . An evaluation window is then formed, with data coming from the six upcoming tests, that is, measurements at t_{R+1}, \dots, t_E , with a mean value of the sample, μ_E . The algorithm progresses by adding the upcoming measurement point, t_{E+1} , to the evaluation window. However, the windows sizes remain constant, which means that the reference window is updated by losing t_0 for the observation made at t_{R+1} , and so on. This technique is made to tackle the non-monotonic behavior of the HI. A disbond propagation index, PI, is flagged with “1”-propagation or “0”-no propagation,

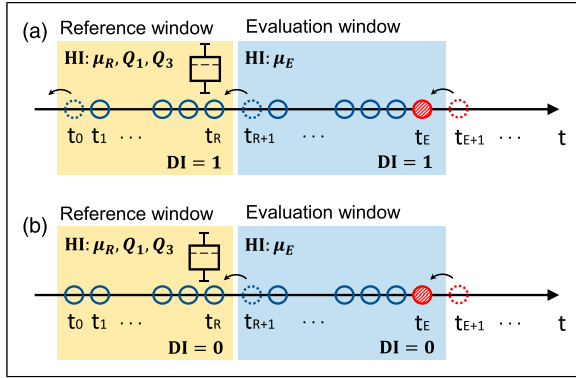


Figure 12. Sliding window technique for the (a) disbond propagation and (b) overall (post-buckling) stiffness degradation identification.

leveraging on boxplot outlier detection as presented in equation (10). The first condition generally expresses outlier detection, based on the boxplot metrics, and is independent of the nature of the reference window data. If any of the relevant data, both in reference and evaluation window, is not labeled with $DI = 1$, the algorithm does not perform disbond propagation check and proceeds to data updating until this requirement is met. Finally, the procedure is repeated for a second consecutive window, which is compared once again to the reference window. If the first condition of equation (10) is again fulfilled, the algorithm yields a final propagation incident at the measurement instance t_E of the second evaluation window. Conclusively, the disbond propagation approach is built in a manner to treat real-time data, with the sole demand the possession of the proper number of data to form the two windows. The length of the windows as well as the number of consecutive evaluations was investigated via trial-and-error checks in order to reduce false positives. However, false positives cannot be precisely measured as we do not have disbond propagation groundtruth throughout the whole test span.

(ii) Regarding stiffness degradation, a similar approach is followed. Now, one difference is that the reference window is constantly increasing by adding new data. Besides this, the greater difference lies in the fact that stiffness degradation is only investigated at sensors which are flagged with $DI = 0$. Essentially, this means that if no local damage is observed, that is, $DI = 0$, a potential global stiffness degradation may be investigated, in the relevant location, as it will alter the strains, as described in “Stiffness degradation” section. By doing this, we avoid the intersection of the two damage types that would have confused the current methodology. Moreover, one more constraint is imposed, namely, a sensing location may be assessed for potential stiffness degradation if the neighboring sensors, along the same foot, fulfill $DI = 0$ for the relevant strain data. The stiffness degradation is predicted based on equation (10). A

stiffness degradation index, SDI, is now used to store the instances whenever degradation of stiffness is estimated, that is, first condition of equation (10), labeling with “1.” In contrary to the disbond propagation, the stiffness degradation is inevitably monotonic. Here lies the reason why the reference window is constantly increasing, as schematically represented in Figure 12(b); we seek to observe changes based on the history of data, as the monotonic decrease of the stiffness progresses. Eventually, the windowing technique, is now implemented for a different window size scheme, namely, initial reference size of 5000 cycles and a constant evaluation size of 5000 cycles, that is, 10 QS tests. As new data are observed, one by one, the reference window increases while the evaluation window propagates with constant size. Similar to the disbond propagation, two consecutive evaluation windows should satisfy the first condition of equation (10) before flagging a stiffness degradation occurrence:

$$PI_i(t_E) = \begin{cases} 1, & \text{if } \mu_E > Q_3 + 1.5(Q_3 - Q_1) \\ \text{or} & \text{if } \mu_E < Q_1 - 1.5(Q_3 - Q_1) \\ 0, & \text{otherwise} \end{cases} \quad (10)$$

$$SDI_i(t_E) = \begin{cases} 1, & \text{if } PI_i(t_E) = 1 \\ 0, & \text{otherwise} \end{cases}$$

Results and discussion

The diagnostic evidence is presented in the current section. The three levels developed previously are coded in MATLAB environment. The conceptual methodology (see Figure 1) is conducted in an automated mode, that is, at first, strains are received from the PT; then, load predictions are made in the DT stage and subsequently features are extracted, which in turn, are post-processed to perform the overall damage diagnosis.

Load predictions

The load predictions for each specimen are presented. The load identification algorithm is evaluated for static strains received per test interval. Namely, one strain value is fed to the algorithm, which corresponds to the maximum load during each QS test.

Several sensors that predict the load have been tested as reference candidates. The performance of the gradient descent is displayed in Figure 13 for all specimens. The groundtruth load is depicted against the deterministic load predictions. The shaded area in the graphs represents the limits of the load predictions, based on which sensor was selected as load evaluator. The scatter points denote the load predictions of the sensor with minimum discordance in comparison to the groundtruth, at every QS test. The predicted load for all cases is in accordance with the actual. Small deviations arise during the last cycles as the stiffness

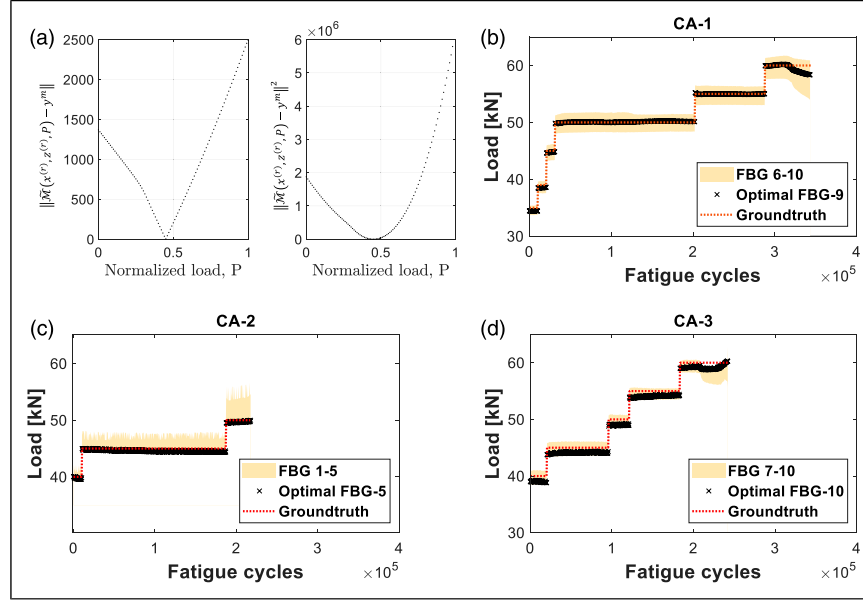


Figure 13. (a) Performance of Euclidean norm and squared norm objective functions, with respect to the normalized load and an observation example y^m . Verification of load predictions made for specimens: (b) CA-1, (c) CA-2, and (d) CA-3.

degradation becomes considerable. The gradient descent robustly performed load prediction and generally needed less than 20 iterations to converge. Random initialization was incorporated within a load range $[0, 70]$ kN. A relative absolute error between two consecutive predictions, was chosen to stop the iterative procedure when it was dropped below a tolerance of 10^{-3} . Moreover, the parameters γ and ϵ were set equal to 10^{-8} and 10^{-4} , respectively. These two parameters should be judiciously selected in order to avoid overshooting of the iterative solution, for example, in cases that γ is significantly large. One more spot worth noting, is the selection of the squared Euclidean norm for objective function in equation (6), F , due to its convex behavior, as shown in Figure 13(a). The load predictions on specimens CA-1, CA-2, and CA-3 are presented in Figure 13(b)–(d), respectively.

Multi-level diagnostics

SSP CA-1. Specimen CA-1 contains an artificially-induced skin/stringer disbond between FBG-1 and FBG-2. Its exact location is reported in Table 3. We recall here that two of the sensors, namely, FBG-1 and FBG-2, had been deliberately placed on the disbond fronts (see Figure 5). Thus, their readings were proved to be too sensitive in any propagation event of the nominal disbond. The disbond presence is successfully detected by the algorithm from the beginning and throughout the test span. More specifically, for the current specimen three sensors exceed the threshold, that is, FBG-1, FBG-2, and FBG-5. The disbond clearly affects only FBG-1 and FBG-2; the last sensor in the disbonded

foot, that is, FBG-5, was diagnosed as detached at an early time and no further actions were made with its strains. On the contrary, the HIs on FBG-6 presented a gradual increase, as it will be shown in the next level of diagnosis.

Regarding the third diagnostic level, it can be seen that the algorithm is concentrated for potential damage propagation type, in the first two sensors, as these are the only sensors labeled with $DI = 1$. More specifically, the first indication regarding propagation is coming from FBG-2, after 10,000 fatigue cycles. However, no observable disbond propagation, obtained via NDT measurements, was estimated during the first 30,000 cycles. The first verification of disbond propagation was made after the first 80,000 fatigue cycles, with an increase in the damaged area from 901.5 mm^2 to 1023.1 mm^2 . When the maximum load of fatigue was increased to -50 kN, it is the most probable moment that disbond actually propagated. This also explains the abrupt drop in the HI behavior of FBG-1 from that moment, which continues until further disbond is verified to has been propagated. So, in a time between 10,000 up to 30,000 cycles, we observe only 10 false indications about propagation of damage from FBG-1 whilst FBG-2 produced 21, as a sudden drop on its HI was observed after 10,500 cycles that inevitably triggered the propagation condition, that is, equation (10). Besides this small number of false alarms, the HI of this sensor produced propagation indications that correspond to actual events, as verified by the NDT evaluation. Here, the fact that the HIs of these two sensors are not monotonic, reveals the complexity of the modified strain field as well as the importance of the windowing technique as followed. As fatigue progresses,

the disbond propagates in the longitudinal directions, which in turn, affects FBG-3 as well as FBG-4. The final evidence of the disbonded area was 2413.9 mm^2 , that is, 62.7% increase, after 341,000 fatigue cycles. Along the bonded foot, all the HIs remained silenced, that is, below the threshold, during the test, besides FBG-6 that after some time presented an increase trend to its HI. Inspections with DolphiCam did not reveal a damage propagation toward the other foot, and thus FBG-6, so, the HI behavior should not be attributed to the propagation of the disbond. However, it was not declared as detached, and thus, we support that potentially is periodically losing its bonding, which may also explain the increased variance observed in the sensor's readings. Finally, stiffness degradation was captured from FBG-10, FBG-8, FBG-7, and FBG-6 (in the early period with $DI = 0$). For the case of FBG-6, though, the imminent increase on its HI misinterprets the stiffness degradation algorithm, leading to degradation predictions that, in reality,

should not be attributed to actual stiffness degradation. The monotonic reduction in the stiffness is experimentally monitored, leading to an overall 9.4% drop, with respect to the initial value. The aggregated performance of multi-level damage diagnosis concept for CA-1 is presented in Figure 14.

SSP CA-2. Specimen CA-2 was impacted at an energy level of 10 J. The nominal disbond area, measured with the DolphiCam, was 1397.9 mm^2 , which spans beneath the region where FBG-6 and FBG-7 are installed. Impact damage presence is detected successfully from the very onset of the test and localization of the damage is realized in the proximity of FBG-6, FBG-7, and FBG-8, as can be seen from Figure 15. From the NDT evidence (see Figure 6) it can be noticed that the disbond never reaches exactly beneath FBG-8. However, the severity of the damage justifies that FBG-8 presents higher values than the threshold. CA-2 was the only specimen with no observable, or classified, sensor detachment.

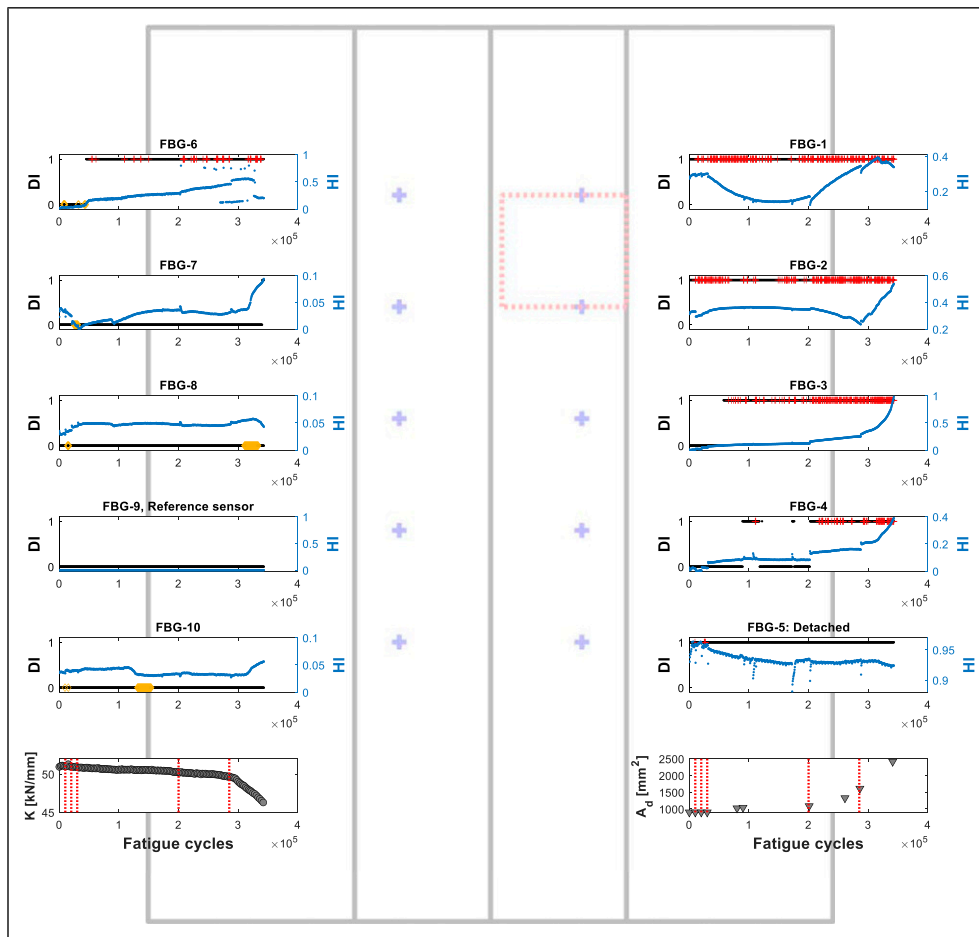


Figure 14. Overall multi-level damage diagnosis for specimen CA-1. Red plus signs (+) indicate the moments when the algorithm produces propagation predictions whereas orange diamonds (◇) indicate stiffness degradation incidents. Experimentally measured stiffness (K) degradation and disbond area (A_d) are plotted with respect to fatigue cycles. Red dotted vertical lines indicate the moment that the limits of maximum fatigue load are increased. (+): Fiber-optic sensors with engraved Bragg gratings, (◇): Teflon insert.

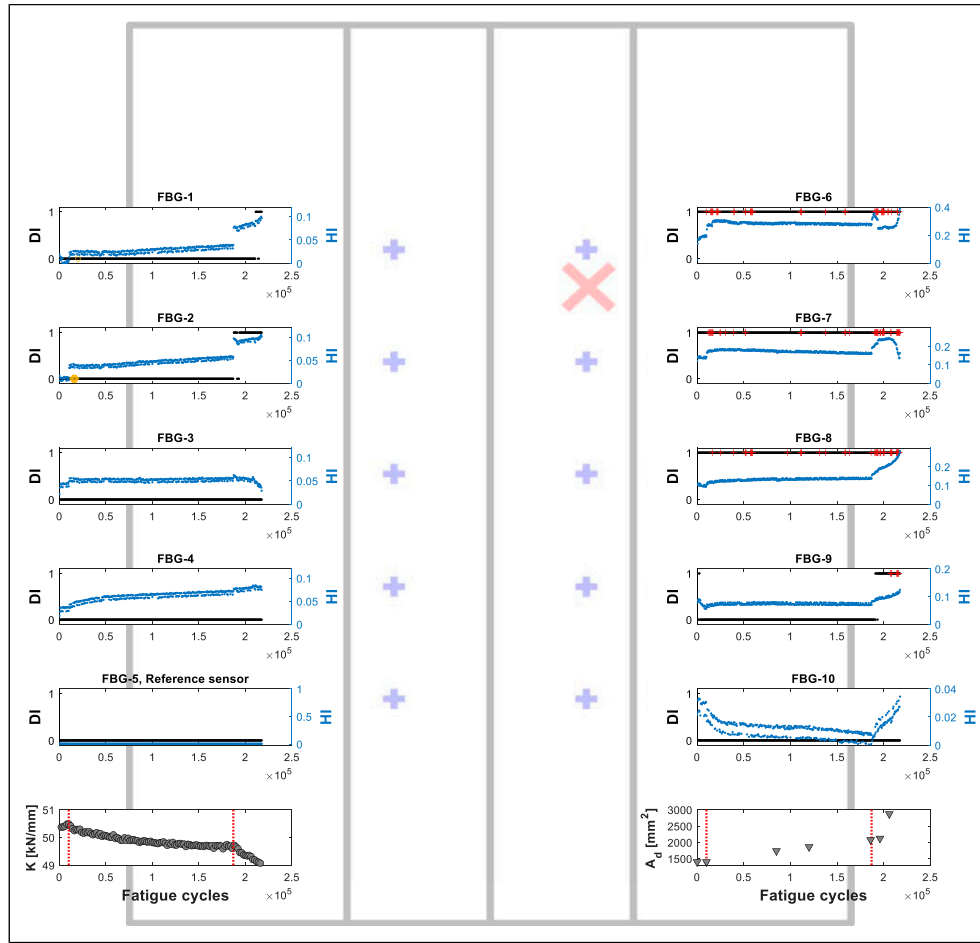


Figure 15. Overall multi-level damage diagnosis for specimen CA-2. Red plus signs (+) indicate the moments when the algorithm produces propagation predictions whereas orange diamonds (◇) indicate stiffness degradation incidents. Experimentally measured stiffness (K) degradation and disbond area (A_d) are plotted with respect to fatigue cycles. Red dotted vertical lines indicate the moment that the limits of maximum fatigue load are increased. (+): FBGs, (X): Impact location.

From the non-destructive inspections, no disbond propagation was observed prior to the first 10,000 cycles. The first measurement that indicated a 19.5% increase in the disbonded area was made at 85,000 cycles. Before the first 10,000 fatigue cycles, the damage type identification algorithm did not produce any predictions of propagation. As the disbond propagation evolved, scatter predictions were produced from the aforementioned damage-affected sensors. This is intensified especially after the last increase in the fatigue maximum load, that is, 187,000 cycles. Once again, sensors lying within the disbonded area, that is, FBGs 6, 7, and 8, develop non-monotonic behaviors, which are attributed to the induced strain modification in the damaged region, as detailed in “Effect of skin-to-stringer disband.” FBG-9 also produced a limited number of disbond propagation events, namely, the first indication coming from this sensor is made at 207,500 cycles. The last inspection was made at 206,000 cycles deriving a disbond area size equal to

2871.8 mm², that is, 51.3% total growth if compared to the nominal area. From stiffness degradation perspective, only a very limited number of indications were produced by the algorithm. However, the overall reduction in stiffness is only 2.6%, small enough to produce large deviation in the HIs labeled with DI = 0. The total findings of the algorithm’s performance are depicted in Figure 15.

SSP CA-3. The second impacted specimen was hit with energy 7.4 J in the skin/stringer border (from the flat skin side), as displayed in Figure 5. The delaminated region at the skin/stringer interface was approximately estimated 232.5 mm² spanning between FBG-1 and FBG-2. Level 1 diagnosis was efficiently achieved again upon failure of the specimen. In Level 2, FBG-1, FBG-6, and a part of FBG-2 indications, presented HIs larger than the threshold. The nominal damage extent does not seem to largely affect the sensor readings until further propagation of the damage was

observed. FBG-1 and FBG-6 were subsequently characterized as detached and any disbond propagation indications coming from these two sensors have not been considered as representative, as discussed in the next diagnostic level.

The induced impact damage was growing relatively slow, until the final increase of the fatigue maximum load. Besides the detached sensors, the only sensors that further detected damage, were FBG-2, FBG-3, and FBG-4 after a certain amount of cycles. First, FBG-2, which was closer to the damage source than the rest of the two sensors, indicated presence as well as propagation of the disbond. The first information related to the existence of damage in FBG-2 was received after 65,000 cycles while the first propagation event was predicted after 108,000 fatigue cycles. The previous estimation of the disbonded area was acquired with a DolpiCam measurement which revealed a 26.1% increase, after 95,000 experienced cycles. Moreover, at some moment, the HI values of this sensor dropped below the

predefined threshold. This can be attributed to the non-monotonic strain field that is developed along the disbonded area, in accordance with the distributions shown in Figure 8. In addition, for FBG-3 and FBG-4 damage is firstly detected after 121,500 and 126,000 cycles, respectively. Finally, after the final increase on the load, further growth was observed in the disbonded area that yielded a monotonic, in that case, trend on the HIs of FBGs 2, 3, and 4. The finally measured area was found 747.8 mm^2 , that is, 68.9% larger than the nominal value. It should be noted here that this measurement was made 30,000 cycles prior to collapse, which means that further growth of the disbond potentially took place. Stiffness degradation was captured from two sensors in the bonded foot, that is, FBG-8 and FBG-9. Two indications of degradation are also produced from FBG-3 in the early stage of testing. The major identification of the stiffness degradation is occurring after 211,500 cycles based on FBG-9 and after 213,500 cycles for readings of FBG-8.

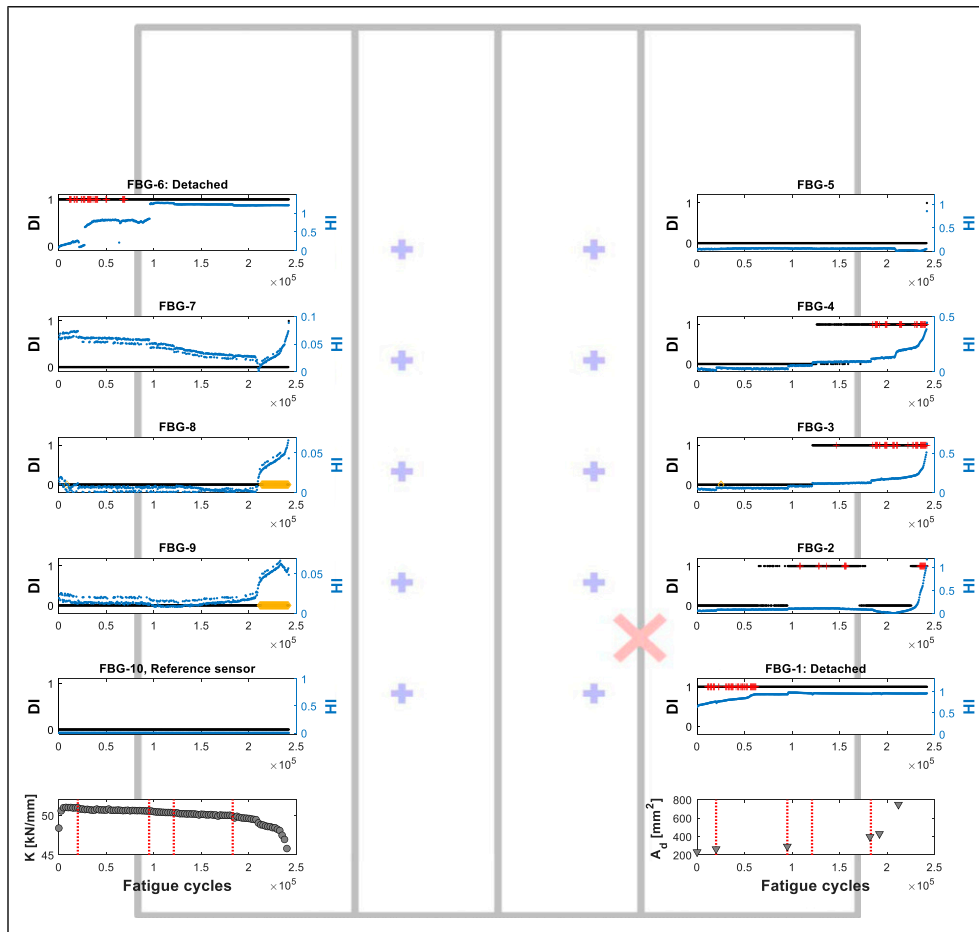


Figure 16. Overall multi-level damage diagnosis for specimen CA-3. Red plus signs (+) indicate the moments when the algorithm produces propagation predictions whereas orange diamonds (◇) indicate stiffness degradation incidents. Experimentally measured stiffness (K) degradation and disbond area (A_d) are plotted with respect to fatigue cycles. Red dotted vertical lines indicate the moment that the limits of maximum fatigue load are increased. (+): FBGs, (x): Impact location.

By the time that degradation is firstly captured from FBG-9, the overall drop on the stiffness was approximately 3.9% whilst the final reduction of the post-buckling stiffness was found to be 10.1%. The performance of the overall diagnosis is presented in Figure 16, for specimen CA-3.

Robustness of the methodology against random loads

The multi-level damage diagnosis results previously presented, were limited in a case of a single strain value received from each sensor, per QS test interval. This strain reflects to the maximum load per test. To check the robustness of the proposed methodology in random loading condition now, we consider a random sample of strains recorded per test. Namely, 100 strains are randomly received per test interval, at various loads lower, but close to the maximum one. This action adds stochasticity on the strain measurements and tests the robustness of the proposed diagnosis concept. After sampling, the following steps remain the same; first, the load is iteratively found, and then, the HIs are calculated based on the predicted load. Figure 17 depicts indicatively the algorithm predictions, per specimen, including the load predictions in accordance with the behavior of the HIs that produced disbond propagation events. Black scatter points represent the HIs' behavior on the case when we have considered only one strain reading (at maximum load) per test. It can be clearly noticed that the trend of the HIs follows the one with the black scatter points even at random loads in the post-buckling regime. Finally, the mean values of the HIs

are estimated, per QS test, and the cumulative propagation and stiffness degradation indications are gathered throughout the test span.

Conclusively, in order to assess the predictions related to disbond propagation as well as (overall) stiffness degradation, the relevant indicators are gathered, per specimen, and expressed as cumulative indications. By doing so, we evaluate the sensitivity of the algorithm's predictions in accordance with the inspection evidence. A vector named cPI, contains the cumulative disbond propagation indications, per cycle. At some instance, if the algorithm predicts propagation in more than one sensor, we consider this as one single indication, stored in a vector oPI, in order to neglect superfluous values. The same procedure is implemented for the overall stiffness degradation with data stored in a vector named oSDI. The overall values are obtained as:

$$\begin{aligned} \text{oPI}(t) &= \begin{cases} 1, & \text{if } \sum_{i=1}^{N_s} PI_i(t) > 0 \\ 0, & \text{if } \sum_{i=1}^{N_s} PI_i(t) = 0 \end{cases} \\ \text{oSDI}(t) &= \begin{cases} 1, & \text{if } \sum_{i=1}^{N_s} SDI_i(t) > 0 \\ 0, & \text{if } \sum_{i=1}^{N_s} SDI_i(t) = 0 \end{cases} \end{aligned} \quad (11)$$

Finally, the cumulative indices are expressed as:

$$\begin{aligned} \text{cPI}(t) &= \sum_{t_0}^t \text{oPI}(t) \\ \text{cSDI}(t) &= \sum_{t_0}^t \text{oSDI}(t) \end{aligned} \quad (12)$$

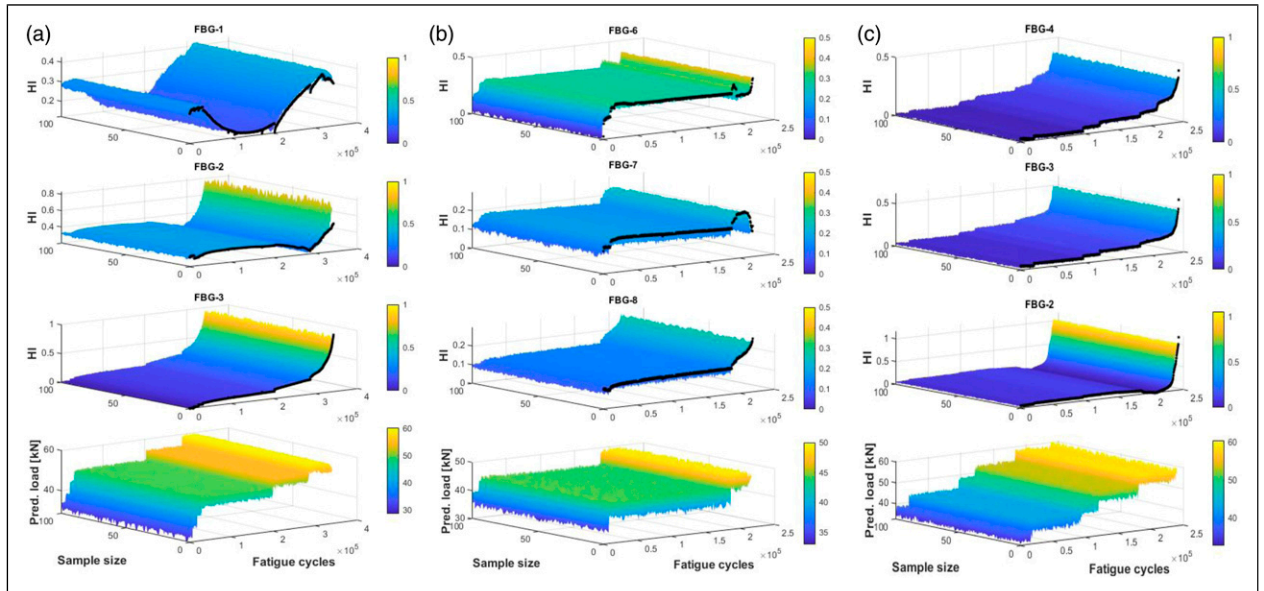


Figure 17. HI samples based on randomly received strains, per test interval, for specimens: (a) CA-1, (b) CA-2, and (c) CA-3. Black scatter points represent the HIs considering strains received from the maximum load per quasi-static test. Note: HI: Health Indicator.

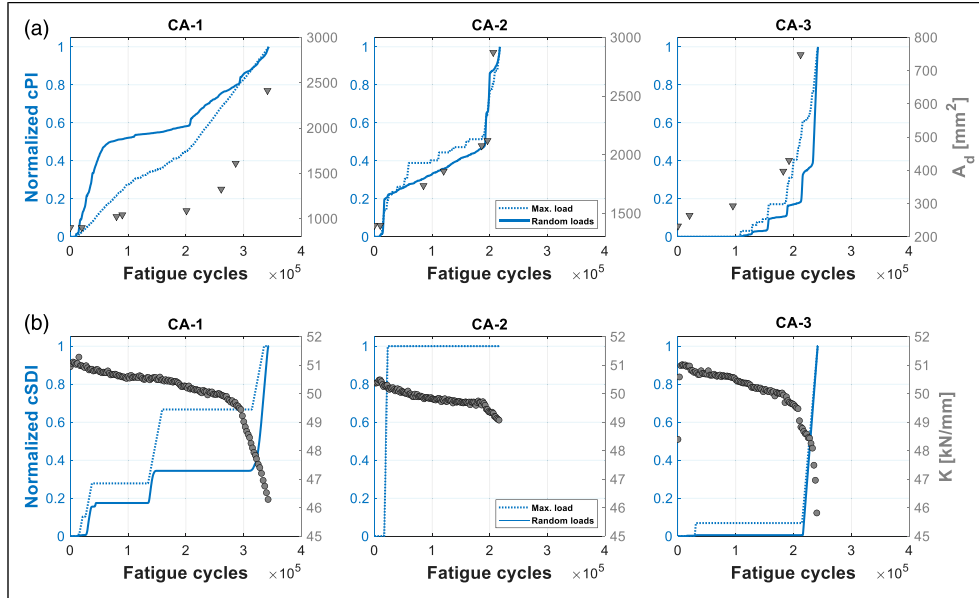


Figure 18. (a) Cumulative disbond propagation and (b) cumulative stiffness degradation predictions, per specimen, accompanied by the measured disbonded area (A_d) and stiffness (K), respectively.

Figure 18(a) depicts the cumulative indications, which are plotted against the relevant phased-array ultrasound measurements of delaminated area, A_d . Both random strains as well as strains received from the maximum load per QS test are considered. Cumulative disbond propagation presents very good agreement with the experimental evidence. The behavior of the cPI is sensitive to the disbond propagation. For specimens CA-2 and CA-3, the detectability is slightly higher when we consider only the maximum strains per QS test. However, for the case of CA-1, a redundancy of propagation indications is predicted in the beginning of the test, for the case of random strains. Figure 18(b) shows the cumulative predictions of stiffness degradation per SSP. Specimen CA-2 is not capable of efficiently capturing the phenomenon, as previously mentioned in “Level 3 diagnostics.” The second impacted specimen, that is, CA-3, is deemed as successful with a sudden increase in the cumulative indications after 207,500 cycles. Specimen CA-1 also provided adequate number of stiffness degradation events until the end of life. The detectability is intensified after 312,000 fatigue cycles and generally higher for the case of strains acquired from the maximum load per test interval.

Conclusion

The proposed SHM methodology introduces a multi-level damage diagnosis approach, applied on aerospace stiffened composite panels. A FE model was developed to represent the pristine baseline of a composite single-stringer panel, which was verified for extensive compressive loading conditions that result in buckling of the panel.

The methodology exploits the premise of strain modification around delaminations with respect to the healthy strain field. The latter is provided in terms of numerically simulated strains acquired from the developed FE model. The longitudinal strains, induced in the locations where real FBGs are installed, are embedded in a RBF surrogate model trained with simulated strains from the FE model. This enhances the feasibility of the methodology, in terms of performing rapid predictions during the period that the algorithm is fed by experimentally received strains.

Prior to feature extraction that enables the damage diagnosis, a properly selected, damage-unaffected, reference sensor was used to predict the load acting on the structure. The reference sensor serves the DT concept, and essentially adapts the behavior of the FE model to the strain data coming from the test. The rest of the sensing locations will be evaluating a HI that assists the diagnostic levels. The damage diagnosis algorithm receives strains from the PT, and evaluates the three diagnostic levels, that is, damage presence, location, and type. For that purpose, three damaged specimens, have been utilized to assess the proposed methodology. Static strains have been periodically acquired from QS test intervals among block loading C-C fatigue cycles. Disbond propagation as well as post-buckling stiffness degradation is monitored during the test.

The first two levels have successfully detected and localized the sources of damage in every panel. Besides that, an extra effort was given to monitor the propagation of the induced skin-to-stringer disbond as well as the stiffness degradation. The evidence of the first type is promising and empowers the proposed methodology. In contrast, stiffness

degradation is not totally captured, especially in cases where minor reduction was observed, for example, specimen CA-2, or unexpected events that may produce false alarms as in specimen CA-1. A limitation of the methodology lies in the fact that the strain modification becomes severe in the post-buckling regime and essentially is not possible to reveal the damage when the structure operates in the linear regime. However, as we have mentioned in the “Introduction” section, these structures are designed to operate and sustain elevated loads that lead to buckling. The authors are currently dedicated to enhancing the present methodology with an additional level, that is, damage quantification, based on an augmented version of the surrogate model incorporating strains from discrete skin/stringer disbond scenarios.

Acknowledgments

The authors would like to acknowledge OPTIMAL STRUCTURAL SOLUTIONS LDA for the manufacturing of the panels, SMARTEC S.A. for the SMARTAPE™ procurement, and our colleagues from University of Patras and Delft University of Technology for their technical support.

Declaration of conflicting interests

The author(s) declared no potential conflicts of interest with respect to the research, authorship, and/or publication of this article.

Funding

The author(s) disclosed receipt of the following financial support for the research, authorship, and/or publication of this article: This work was supported by the European Union’s Horizon 2020 research and innovation programme ReMAP (Grant Agreement Number: 769288).

ORCID iDs

Dimitrios Milanoski  <https://orcid.org/0000-0003-1995-5387>
Georgios Galanopoulos  <https://orcid.org/0000-0003-4998-1308>

References

- Vickers M and Grieves J. Digital Twin: Mitigating Unpredictable, Undesirable Emergent Behavior in Complex Systems. In: *Transdisciplinary Perspectives on Complex Systems: New Findings and Approaches*. Cham: Springer, 2016, pp. 85–113.
- Wagg DJ, Worden K, Barthorpe RJ, et al. Digital twins: state-of-the-art and future directions for modeling and simulation in engineering dynamics applications. *ASCE-ASME J Risk Uncertain Eng Syst B: Mech Eng* 2020; 6(3): 030901.
- Niederer SA, Sacks MS, Girolami M, et al. Scaling digital twins from the artisanal to the industrial. *Nat Comput Sci* 2021; 1(5): 313–320.
- Tuegel EJ, Ingrassia AR, Eason TG, et al. Reengineering aircraft structural life prediction using a digital twin. *Int J Aerosp Eng* 2011; 2011: 1–14.
- Seshadri BR and Krishnamurthy T. Structural health management of damaged aircraft structures using the digital twin concept. In: 25th AIAA/AHS Adaptive Structures Conference, Grapevine, Texas, 9–13 January 2017.
- Reifsnider K and Majumdar P. Multiphysics stimulated simulation digital twin methods for fleet management. In: 54th AIAA/ASME/ASCE/AHS/ASC Structures, Structural Dynamics, and Materials Conference, Boston, Massachusetts, 8–11 April 2013.
- Kraft EM. The US air force digital thread/digital Twin – life cycle integration and use of computational and experimental knowledge. In: 54th AIAA Aerospace Sciences Meeting, San Diego, California, USA, 4–8 January 2016.
- Worden K, Cross EJ, Barthorpe RJ, et al. On digital twins, mirrors, and virtualizations: frameworks for model verification and validation. *ASCE-ASME J Risk Uncertain Eng Syst B: Mech Eng* 2020; 6(3): 030902.
- Glaessgen EH and Stargel DS. The digital twin paradigm for future NASA and U.S. air force vehicles. In: 53rd AIAA/ASME/ASCE/AHS/ASC Structures, Structural Dynamics and Materials Conference, Honolulu, Hawaii, 23–26 April 2012.
- Singh V and Willcox KE. Engineering design with digital thread. *AIAA J* 2018; 56(11): 4515–4528.
- AIAA. Digital Twin: Definition & Value. *An AIAA and AIA Position Paper*. AIAA, 2020, pp. 1–16.
- Boller C and Buderath M. Fatigue in aerostructures—where structural health monitoring can contribute to a complex subject. *Philos Trans A Math Phys Eng Sci* 2007; 365(1851): 561–587.
- Pascoe JA. Slow-growth damage tolerance for fatigue after impact in FRP composites: why current research won’t get us there. *Theor Appl Fract Mech* 2021; 116: 103127.
- Falcatelli F, Yue N, Di Sante R, et al. Probability of detection, localization, and sizing: the evolution of reliability metrics in Structural Health Monitoring. *Struct Health Monit* 2021; 14759217211060780.
- Eleftheroglou N and Loutas T. Fatigue damage diagnostics and prognostics of composites utilizing structural health monitoring data and stochastic processes. *Struct Health Monit* 2016; 15(4): 473–488.
- Keane A, Forrester A and Sobester A. *Engineering Design via Surrogate Modelling: A Practical Guide*. Washington, DC: American Institute of Aeronautics and Astronautics, Inc., 2008.
- Tsialamanis G, Wagg DJ, Dervilis N, et al. On generative models as the basis for digital twins. *Data-Centric Eng* 2021; 2: e11.
- Ritto TG and Rochinha FA. Digital twin, physics-based model, and machine learning applied to damage detection in structures. *Mech Syst Signal Pr* 2021; 155: 107614.
- Leser PE, Hochhalter JD, Warner JE, et al. Probabilistic fatigue damage prognosis using surrogate models trained via three-dimensional finite element analysis. *Struct Health Monit* 2017; 16(3): 291–308.

20. Sbarufatti C, Manes A and Giglio M. Performance optimization of a diagnostic system based upon a simulated strain field for fatigue damage characterization. *Mech Syst Signal Pr* 2013; 40(2): 667–690.
21. Ye Y, Yang Q, Yang F, et al. Digital twin for the structural health management of reusable spacecraft: a case study. *Eng Fract Mech* 2020; 234: 107076.
22. Kapteyn MG, Knezevic DJ, Huynh DB, et al. Data-driven physics-based digital twins via a library of component-based reduced-order models. *Int J Numer Methods Eng* 2022; 123: 2986–3003. nme.6423.
23. Cristiani D, Sbarufatti C, Cadini F, et al. Fatigue damage diagnosis and prognosis of an aeronautical structure based on surrogate modelling and particle filter. *Struct Health Monit* 2020; 147592172097155.
24. Cristiani D, Sbarufatti C and Giglio M. Damage diagnosis and prognosis in composite double cantilever beam coupons by particle filtering and surrogate modelling. *Struct Health Monit* 2021; 20(3): 1030–1050.
25. Seventekidis P, Giagopoulos D, Arailopoulos A, et al. Structural Health Monitoring using deep learning with optimal finite element model generated data. *Mech Syst Signal Pr* 2020; 145: 106972.
26. Karve PM, Guo Y, Kapusuzoglu B, et al. Digital twin approach for damage-tolerant mission planning under uncertainty. *Eng Fract Mech* 2020; 225: 106766.
27. Giannakeas IN, Sharif Khodaei Z and Aliabadi M. Digital clone testing platform for the assessment of SHM systems under uncertainty. *Mech Syst Signal Pr* 2022; 163: 108150.
28. Booyse W, Wilke DN and Heyns S. Deep digital twins for detection, diagnostics and prognostics. *Mech Syst Signal Pr* 2020; 140: 106612.
29. Millwater H, Ocampo J and Crosby N. Probabilistic methods for risk assessment of airframe digital twin structures. *Eng Fract Mech* 2019; 221: 106674.
30. Leser PE, Warner JE, Leser WP, et al. A digital twin feasibility study (Part II): non-deterministic predictions of fatigue life using in-situ diagnostics and prognostics. *Eng Fract Mech* 2020; 229: 106903.
31. Liao M, Renaud G and Bombardier Y. Airframe digital twin technology adaptability assessment and technology demonstration. *Eng Fract Mech* 2020; 225: 106793.
32. Giannaros E, Kotzakolios A, Kostopoulos V, et al. Low- and high-fidelity modeling of sandwich-structured composite response to bird strike, as tools for a digital-twin-assisted damage diagnosis. *Int J Impact Eng* 2021; 160: 104058.
33. Taylor SG, Park G, Farinholt KM, et al. Fatigue crack detection performance comparison in a composite wind turbine rotor blade. *Struct Health Monit* 2013; 12(3): 252–262.
34. Augustyn D, Ulriksen MD and Sørensen JD. Reliability updating of offshore wind substructures by use of digital twin information. *Energies (Basel)* 2021; 14(18): 5859.
35. Anyfantis KN. An abstract approach toward the structural digital twin of ship hulls: a numerical study applied to a box girder geometry. *Proc Inst Mech Eng M: J Eng Marit Environ* 2021; 235(3): 718–736.
36. Silionis NE and Anyfantis KN. Static strain-based identification of extensive damages in thin-walled structures. *Struct Health Monit* 2021; 147592172110506.
37. Worden K, Farrar CR, Manson G, et al. The fundamental axioms of structural health monitoring. *Proc Math Phys Eng Sci* 2007; 463(2082): 1639–1664.
38. Di Sante R. Fibre optic sensors for structural health monitoring of aircraft composite structures: recent advances and applications. *Sensors* 2015; 15(8): 18666–18713.
39. Güemes A, Fernández-López A, Díaz-Maroto PF, et al. Structural health monitoring in composite structures by fiber-optic sensors. *Sensors (Basel)* 2018; 18(4): 1094.
40. Hill KO and Meltz G. Fiber Bragg grating technology fundamentals and overview. *J Lightwave Technol* 1997; 15(8): 1263–1276.
41. Yeager M, Todd M, Gregory W, et al. Assessment of embedded fiber Bragg gratings for structural health monitoring of composites. *Struct Health Monit* 2017; 16(3): 262–275.
42. Loutas TH, Charlaftis P, Airoidi A, et al. Reliability of strain monitoring of composite structures via the use of optical fiber ribbon tapes for structural health monitoring purposes. *Compos Struct* 2015; 134: 762–771.
43. Palaniappan J, Ogin SL, Thorne AM, et al. Disbond growth detection in composite-composite single-lap joints using chirped FBG sensors. *Compos Sci Technol* 2008; 68(12): 2410–2417.
44. Yashiro S, Wada J and Sakaida Y. A monitoring technique for disbond area in carbon fiber-reinforced polymer bonded joints using embedded fiber Bragg grating sensors: development and experimental validation. *Struct Health Monit* 2017; 16(2): 185–201.
45. Katsikeros CE and Labeas GN. Development and validation of a strain-based Structural Health Monitoring system. *Mech Syst Signal Pr* 2009; 23(2): 372–383.
46. Kamath GM, Sundaram R, Gupta N, et al. Damage studies in composite structures for structural health monitoring using strain sensors. *Struct Health Monit* 2010; 9(6): 497–512.
47. Panopoulou A, Roulias D, Loutas TH, et al. Health monitoring of aerospace structures using fibre Bragg gratings combined with advanced signal processing and pattern recognition techniques. *Strain* 2012; 48(3): 267–277.
48. Loutas TH and Bourikas A. Strain sensors optimal placement for vibration-based structural health monitoring. The effect of damage on the initially optimal configuration. *J Sound Vib* 2017; 410: 217–230.
49. Li HC, Herszberg I and Mouritz AP. Automated characterization of structural disbonds by statistical examination of bond-line strain distribution. *Struct Health Monit* 2006; 5(1): 83–94.
50. Kesavan A, John S and Herszberg I. Strain-based structural health monitoring of complex composite structures. *Struct Health Monit* 2008; 7(3): 203–213.
51. Takeda Si, Aoki Y and Nagao Y. Damage monitoring of CFRP stiffened panels under compressive load using FBG sensors. *Compos Struct* 2012; 94(3): 813–819.

52. Terroba F, Frövel M and Atienza R. Structural health and usage monitoring of an unmanned turbojet target drone. *Struct Health Monit* 2019; 18(2): 635–650.
53. Alvarez-Montoya J, Carvajal-Castrillón A and Sierra-Pérez J. In-flight and wireless damage detection in a UAV composite wing using fiber optic sensors and strain field pattern recognition. *Mech Syst Signal Pr* 2020; 136: 106526.
54. Milanoski D, Galanopoulos G, Broer A, et al. A strain-based health indicator for the shm of skin-to-stringer disbond growth of composite stiffened panels in fatigue. In: Rizzo P, Milazzo A and Milazzo A (eds). Proceedings of the 10th European Workshop on Structural Health Monitoring (EWSHM), Palermo, Italy, 6–9 July 2020. Springer, Cham, pp. 626–635. Lecture Notes in Civil Engineering, vol 127.
55. Panopoulou A, Loutas T, Roulias D, et al. Dynamic fiber Bragg gratings based health monitoring system of composite aerospace structures. *Acta Astronaut* 2011; 69(7–8): 445–457.
56. Anastasopoulos D, De Smedt M, Vandewalle L, et al. Damage identification using modal strains identified from operational fiber-optic Bragg grating data. *Struct Health Monit* 2018; 17(6): 1441–1459.
57. Milanoski DP and Loutas TH. Strain-based health indicators for the structural health monitoring of stiffened composite panels. *J Intell Mater Syst Struct* 2021; 32(3): 255–266.
58. Milanoski DP, Galanopoulos GK and Loutas TH. Digital-Twins of composite aerostructures towards Structural Health Monitoring. In: 2021 IEEE 8th International Workshop on Metrology for AeroSpace (MetroAeroSpace), Naples, Italy, 23–25 June 2021, pp. 613–618.
59. Goossens S, Berghmans F, Muñoz K, et al. A global assessment of barely visible impact damage for CFRP sub-components with FBG-based sensors. *Compos Struct* 2021; 272: 114025.
60. Richstein R, Reichartz T, Janetzko-Preisler A, et al. Methodical development of a structural health monitoring system for COPV supported by a digital shadow. In: VIII Conference on Mechanical Response of Composites, 22–24 September 2021/Online event. CIMNE, 2021.
61. Ciminello M, Concilio A, Galasso B, et al. Skin-stringer debonding detection using distributed dispersion index features. *Struct Health Monit* 2018; 17(5): 1245–1254.
62. Grassia L, Iannone M, Califano A, et al. Strain based method for monitoring the health state of composite structures. *Compos B Eng* 2019; 176: 107253.
63. Broer A, Galanopoulos G, Benedictus R, et al. Fusion-based damage diagnostics for stiffened composite panels. *Struct Health Monit* 2021; 147592172110071.
64. Galanopoulos G, Milanoski D, Broer AAR et al. Health indicators for diagnostics and prognostics of composite aerospace structures. In: 2021 IEEE 8th International Workshop on Metrology for AeroSpace (MetroAeroSpace), Naples, Italy, 23–25 June 2021, pp. 541–546.
65. Galanopoulos G, Milanoski D, Broer A, et al. Health monitoring of aerospace structures utilizing novel health indicators extracted from complex strain and acoustic emission data. *Sensors* 2021; 21(17): 5701.
66. Bergmayr T, Winklberger M, Kralovec C, et al. Structural health monitoring of aerospace sandwich structures via strain measurements along zero-strain trajectories. *Eng Fail Anal* 2021; 126: 105454.
67. Winklberger M, Kralovec C and Schagerl M. Development of aircraft spoiler demonstrators for cost-efficient investigations of SHM technologies under quasi-realistic loading conditions. *Aerospace* 2021; 8(11): 320.
68. Colombo L, Sbarufatti C and Giglio M. Definition of a load adaptive baseline by inverse finite element method for structural damage identification. *Mech Syst Signal Pr* 2019; 120: 584–607.
69. Colombo L, Oboe D, Sbarufatti C, et al. Shape sensing and damage identification with iFEM on a composite structure subjected to impact damage and non-trivial boundary conditions. *Mech Syst Signal Pr* 2021; 148: 107163.
70. Kefal A and Tessler A. Delamination damage identification in composite shell structures based on Inverse Finite Element Method and Refined Zigzag Theory. In: *Developments in the Analysis and Design of Marine Structures*. Trondheim, Norway, 7–9 June 2021: CRC Press, 2021, pp. 354–363.
71. Bisagni C, Vescovini R and Dávila CG. Single-stringer compression specimen for the assessment of damage tolerance of postbuckled structures. *J Aircr* 2011; 48(2): 495–502.
72. Dávila CG and Bisagni C. Fatigue life and damage tolerance of postbuckled composite stiffened structures with initial delamination. *Compos Struct* 2017; 161: 73–84.
73. Zhang J and Bisagni C. Buckling-driven mechanisms for twisting control in adaptive composite wings. *Aerosp Sci Technol* 2021; 118: 107006.
74. Cawley P. Structural health monitoring: Closing the gap between research and industrial deployment. *Struct Health Monit* 2018; 17(5): 1225–1244.
75. Krueger R. Development and application of benchmark examples for mixed-mode i/ii quasi-static delamination propagation predictions. In: 27th Annual Technical Conference of the American Society for Composites 2012, Held Jointly with 15th Joint US-Japan Conference on Composite Materials and ASTM-D30 Meeting, Arlington, Texas, USA, 1–3 October 2012, pp. 83–101.
76. Dassault Systèmes Simulia Corp. *Abaqus Analysis User's Manual Guide*. Providence, RI, 2021.
77. Yue N, Broer A, Briand W, et al. Assessing stiffness degradation of stiffened composite panels in post-buckling compression-compression fatigue using guided waves. *Compos Struct* 2022; 293: 115751.
78. Prawin J, Lakshmi K and Rao ARM. Structural damage diagnosis under varying environmental conditions with very limited measurements. *J Intell Mater Syst Struct* 2020; 31(5): 665–686.
79. Yue N, Khodaei ZS and Aliabadi MH. Damage detection in large composite stiffened panels based on a novel SHM building block philosophy. *Smart Mater Struct* 2021; 30(4): 045004.